

The multifunctionality of lanthanum-strontium cobaltite nanopowder: high-pressure magnetic and excellent electrocatalytic properties for OER

Hanlin Yu^a, N.A. Liedienov^{a,b,*}, I.V. Zatovsky^c, D.S. Butenko^{d,e,*}, I.V. Fesych^f, Wei Xu^g,
Songchun Rui^h, Quanjun Li^a, Bingbing Liu^a, A.V. Pashchenko^{a,c,i}, G.G. Levchenko^{a,c,*}

^aState Key Laboratory of Superhard Materials, International Center of Future Science, Jilin University, 130012 Changchun, P.R. China

^bDonetsk Institute for Physics and Engineering named after O.O. Galkin, NASU, 03028 Kyiv, Ukraine

^cF.D. Ovcharenko Institute of Biocolloidal Chemistry, NASU, 03142 Kyiv, Ukraine

^dShenzhen Key Laboratory of Solid State Batteries, Southern University of Science and Technology, Shenzhen 518055, P.R. China

^eAcademy for Advanced Interdisciplinary Studies, Southern University of Science and Technology, Shenzhen 518055, P.R. China

^fTaras Shevchenko National University of Kyiv, 01030 Kyiv, Ukraine

^gState Key Laboratory of Inorganic Synthesis and Preparative Chemistry, College of Chemistry, Jilin University, Changchun, 130012, P.R. China

^hBaicheng Normal University, 137099 Baicheng, China

ⁱInstitute of Magnetism NASU and MESU, 03142 Kyiv, Ukraine

*Corresponding author

E-mail address: nikita.ledenev.ssp@gmail.com (N.A. Liedienov)

debut98@ukr.net (D.S. Butenko)

g-levch@ukr.net (G.G. Levchenko)

Abstract

Simultaneous study of magnetic and electrocatalytic properties of cobaltites under extreme conditions expands understanding of physical and chemical processes proceeding in them with the possibility of their further practical application. Therefore, $\text{La}_{0.6}\text{Sr}_{0.4}\text{CoO}_3$ (LSCO) nanopowders have been synthesized at different annealing temperatures $t_{\text{ann}} = 850, 875, 900$ °C, and their multifunctional properties have been studied comprehensively. As t_{ann} increases, the rhombohedral (sp. gr. $R\bar{3}c$) perovskite structure of the LSCO becomes more single-phase, whereas average particle size and dispersion grow. Co ions are in mixed valence states, including major Co^{3+} and Co^{4+} components. It has been found that the LSCO-900 shows two main Curie temperatures, T_{C1} and T_{C2} , associated with a particle size distribution. As an external hydrostatic pressure P increases, average $\langle T_{C1} \rangle$ and $\langle T_{C2} \rangle$ increase from 253 and 175 K under ambient pressure to 268 and 180 K under $P = 0.8$ GPa, respectively. At the same time, the antiferromagnetic temperature T_{AFM} and blocking temperature T_B also increase from 145 and 169 K to 158 and 170 K, respectively. The increment of $\langle dT_C/dP \rangle$ for the smaller and bigger particles is sufficiently high and equals 10 and 13 K/GPa, respectively. The magnetocaloric effect in the LSCO-900 nanopowder is relatively weak but with an extremely wide peak $\delta T_{\text{FWHM}} > 50$ K that makes this composition interesting to be used as one of the components of the composite expanding its working temperature window. Moreover, all LSCO samples showed excellent electrocatalytic performance for the overall water splitting (OER) process (overpotentials only 265–285 mV at a current density of 10 mA cm^{-2}) with minimal η_{10} for LSCO-900. Based on the XPS data, it was found that the formation of a dense amorphous layer on the surface of the particles ensures high stability as a catalyst (at least 24 h) during electrolysis in 1 M KOH electrolyte.

Keywords: cobaltites; nanopowder; high pressure magnetic studies; OER; electrochemistry

1. Introduction

Interest in lanthanum-doped strontium $\text{La}_{1-x}\text{Sr}_x\text{CoO}_3$ cobaltites is constantly increasing due to their physical and chemical multifunctionality [1-5]. They demonstrate unique magnetic and transport properties [6, 7], as well as charge, spin, and orbital ordering [8], spin-state transitions [9], electromagnetic phase separation [10], and metal-insulator transitions [11] with strong mutual spin, orbital, charge, and lattice coupling [12]. It makes them ferromagnetic (FM), ferroelectric, and electrocatalytically active with high electrode performance and giant magnetoresistance effect [13, 14]. Moreover, they show high ionic and electronic conductivity, good catalytic properties, and high stability [15], especially because of the low mobility of Sr on the crystal surface and the formation of Co^{4+} ions and oxygen vacancies [16]. All these attract great scientific interest to cobaltites and make them promising candidates for their practical application as electrode materials for high-temperature solid oxide fuel cells, catalysts, current and magnetic field sensors, gas sensors, etc. [17-23]. However, there are still unclear and unstudied physical and chemical processes as the surface-dependent reasons for obtaining high electrode performance and the influence of high external hydrostatic pressure on the magnetic phase transitions and magnetocaloric effect (MCE).

Original LaCoO_3 has an antiferromagnetic (AFM) order, and dilution with divalent Sr^{2+} up to $x = 0.4$ enhance its FM order making this $\text{La}_{0.6}\text{Sr}_{0.4}\text{CoO}_3$ compound fully FM with the highest Curie temperature $T_C \approx 230$ K and the closest to the room temperature among other $\text{La}_{1-x}\text{Sr}_x\text{CoO}_3$ compositions [11]. However, the T_C can significantly differ and be 246 K [7, 24] or even 321 K [25] for the same $x = 0.4$. Moreover, besides classical FM double-exchange (DE) between Co^{3+} and Co^{4+} ions, the AFM superexchange interactions $\text{Co}^{3+}-\text{Co}^{3+}$ and $\text{Co}^{4+}-\text{Co}^{4+}$, and phase separation can coexist [26] that makes this $\text{La}_{0.6}\text{Sr}_{0.4}\text{CoO}_3$ system more complicated along with the sophisticated spin states distribution. Additionally, there is no data about particle size distribution's influence on the magnetic properties, Curie temperature, and MCE of the $\text{La}_{0.6}\text{Sr}_{0.4}\text{CoO}_3$ nanopowders. The effect of high hydrostatic pressure on their functional properties is of particular interest. External pressure should modify Co–O distance and Co–O–Co angle and, as a result, change exchange interactions, phase

transition temperatures, degree of magnetic uniformity, and MCE parameters. All these issues and unspecified moments need to be clarified.

Among the various functional properties of materials-based perovskite oxides, including 3d-metals (Mn, Fe, Co, Ni), a promising electrocatalytic activity toward oxygen evolution should also be noted [27]. It fully applies to Ln- and Co-containing complex oxides of the ABO_3 -type, where for perovskites, A -positions usually correspond to a rare-earth or alkaline earth element, and B is commonly a transition metal or a combination thereof [28-37]. In general, it is considered that the oxygen-catalytic activity of perovskites is influenced by both types of metal in the A - and B -sites [38]. However, the high electrocatalytic activity of perovskites for overall water splitting (OER) in an alkaline medium is primarily the result of the redox behavior of the hybridization of transition metal 3d and oxygen 2p orbitals [39]. Numerical studies of perovskites as electrocatalysts revealed that, in addition to the chemical composition, activity in oxygen electrocatalysis reactions is also affected by a significant number of factors, namely: method and conditions of preparation of the material (annealing at different temperatures and in a controlled atmosphere can cause different types of defects on the surface) [31, 40]; particle size, porosity, and shape (affects active surface area) [29-31, 41]; doping [28, 32, 34, 42, 43]; amorphization of the surface [44]. Moreover, due to electrochemical processes or an aggressive alkaline electrolyte, complex oxides, including perovskites, can be transformed *in situ* to other compounds [45-47], directly affecting the electrocatalytic activity during long-term electrolysis. Accordingly, when studying perovskites as electrocatalysts for OER, evaluating their primary activity and conducting research after electrochemical testing is crucial.

Additionally, studying electrochemical activity and physical properties directly on the same samples is very important since the obtained data supplements each other and allows us to make more correct conclusions. Moreover, knowledge of the behavior of other physical properties, such as temperature changes of magnetic phase transitions and magnetoactive phenomena (MCE or magnetoresistance effect) under changing internal and external factors, is essential as well when it is necessary to change the conditions of electrocatalytic applications.

Thus, in this paper, the cobaltite $\text{La}_{0.6}\text{Sr}_{0.4}\text{CoO}_3$ nanopowders have been obtained under different annealing temperatures $t_{\text{ann}} = 850, 875, \text{ and } 900 \text{ }^\circ\text{C}$ and their structure, morphology, particle size distribution, as well as magnetic, magnetocaloric, and electrocatalytic properties have been studied comprehensively. The most single-phase $\text{La}_{0.6}\text{Sr}_{0.4}\text{CoO}_3$ nanopowder with $t_{\text{ann}} = 900 \text{ }^\circ\text{C}$ has been selected to study the phase transitions and magnetic properties under high hydrostatic pressure up to $P \approx 0.8 \text{ GPa}$. The same sample showed excellent electrocatalytic activity and high stability for OER in alkaline electrolytes.

2. Experimental section

2.1. Sample preparation

Cobaltite $\text{La}_{0.6}\text{Sr}_{0.4}\text{CoO}_3$ (LSCO) nanopowders were obtained using the sol-gel method from the initial $\text{La}(\text{NO}_3)_3 \cdot 6\text{H}_2\text{O}$ (99.9% trace metals basis, Sigma–Aldrich), $\text{Sr}(\text{NO}_3)_2$ (ACS reagent, $\geq 99.0\%$, Sigma–Aldrich) and $\text{Co}(\text{NO}_3)_2 \cdot 6\text{H}_2\text{O}$ (reagent grade, 98%, Sigma–Aldrich) reagents. The calculated amount of nitrates and citric acid (the ratio of the molar sum of metals and $\text{H}_3\text{Cit} \cdot \text{H}_2\text{O}$ was 1:1) were dissolved in deionized water. The solution was evaporated to form a homogeneous gel, which was dehydrated and heated from 200 to 500 $^\circ\text{C}$ (the heating rate equals 50 $^\circ\text{C} \cdot \text{h}^{-1}$). The obtained powder was ground in an agate mortar and annealed at temperatures $t_{\text{ann}} = 850, 875, \text{ and } 900 \text{ }^\circ\text{C}$ for 10 h at each temperature. Finally, three samples obtained at different t_{ann} were named LSCO-850, LSCO-875, and LSCO-900 for further investigation.

2.2. Characterization

The phase composition and size of coherent scattering regions of the samples were examined using the X-ray diffraction (XRD) method on a Shimadzu LabX XRD-6000 diffractometer in $\text{CuK}\alpha_1$ -radiation ($\lambda = 0.15406 \text{ nm}$) before electrocatalysis and X-ray diffractometer MicroMax-007 HF (Rigaku, Japan) in $\text{Mo-K}\alpha$ radiation ($\lambda = 0.071146 \text{ nm}$) after electrocatalysis, both at room temperature. The database JCPDS PDF-2 was used for defining the phase composition. The

refinement of crystal structures was carried out with Rietveld analysis^[48] using FullProf software^[49].

The morphology and size of particles were determined using the transmitting electron microscope (TEM) method on a JEM-2200FS Transmission Electron Microscope and scanning electron microscope (SEM) method on a FEI MAGELLAN 400 and Bruker XFlash 6|60 in the Hitachi Regulus 8100. The distribution function of nanoparticle size was obtained by analyzing SEM and TEM images using Nano Measure 1.2.5 software^[45]. Additionally, the chemical composition of the samples was clarified using energy-dispersive X-ray spectroscopy (EDS) mode.

X-ray photoelectron spectroscopy (XPS) measurements were performed on an ESCALAB 250 X-ray photoelectron spectrometer. The XPS spectra were fitted and analyzed using OriginPro 2018 software. The background of the X-ray photoelectronic lines was cut using the Shirley method. The spectra were excited using monochromatized Al-K α radiation. The state of the surfaces was monitored through the C1s line, allowing calibration of the energy scales for all spectra. The C1s line binding energy was approximately 285 eV.

Magnetic measurements were carried out using a Quantum Design SQUID MPMS 3 in a temperature range from 2 to 300 K and in a magnetic field up to 30 kOe. The temperature dependences of magnetization $M(T)$ under $H = 50$ Oe were carried out in two regimes: zero-field cooling (ZFC) and field cooling (FC). The heating and cooling of samples were carried out with a constant rate of $1 \text{ K} \cdot \text{min}^{-1}$. The MCE was determined using magnetization isotherms $M(H)$ near Curie temperature T_C with a $\Delta T = 2$ K step. Each isotherm $M(H)$ was measured with an increase in the magnetic field H from 0 to 10 kOe with a step of $\Delta H = 100$ Oe. Before each measurement of isotherms, magnetic nanopowder was demagnetized. Additionally, magnetic measurements under high pressure up to $P \approx 0.8$ GPa were performed using a piston-type pressure cell made of Ni–Cr–Al alloy^[50, 51]. Silicon oil of low viscosity was used as a pressure-transmitting medium. The pressure inside was measured using the pressure dependence of the superconducting transition temperature of high-purity lead.

2.3. Electrodes fabrication and electrochemical measurements

To fabricate the working electrodes, mixtures of LSCO samples, Super P (conductive carbon black), and PVDF (polyvinylidene fluoride) were prepared in a weight ratio of 85:10:5, respectively. Next, NMP (N-methylpyrrolidone) was added to the mixture. After that, the liquid suspension was applied onto a carbon fiber (HCP331N) with a working area of 1 cm² and dried at 60 °C for 24 h in a vacuum oven. Each electrode contained approximately about 30 mg of an electroactive material. The benchmark RuO₂/C electrode for investigating OER was made using a similar preparation procedure.

The electrochemical tests were conducted using the electrochemical workstation (CHI 760E, Shanghai, China). A typical three-electrode setup included an LSCO working electrode, a commercial Hg/HgO reference electrode, and a platinum foil counter electrode in 1M KOH (pH = 14). The linear sweep voltammetry (LSV) curves were collected at a scan rate of 1 mV·s⁻¹ with iR-compensation. Electrochemical impedance spectroscopy (EIS) was obtained in a frequency range from 0.1 to 100 kHz with an amplitude of 5 mV at the open circuit potential. Chronopotentiometry (CP) was carried out under a constant current density of 10 mA·cm⁻² for 24 h. All the potentials versus Hg/HgO were converted to versus reversible hydrogen electrode (RHE): ($E_{\text{RHE}} = E_{\text{Hg/HgO}} + 0.098 + 0.059 \times \text{pH}$).

3. Results and discussion

3.1. Structural properties

XRD patterns of the LSCO nanopowders are presented in Fig. 1. The main crystalline phase is a perovskite crystal structure with a rhombohedral $R\bar{3}c$ space group. Some of the second-phase was also detected as SrCo_{0.78}O_{2.48}, which decreases with increasing t_{ann} from 17.4% for LSCO-850 to 14.8% for LSCO-875 and 8% for LSCO-900. It should be noted that this impurity with increased content of cationic "Co_{0.78}" and anionic "O_{2.48}" vacancies does not influence the magnetic properties of the main LSCO phase near its high Curie temperature $T_C \approx 250$ K (see the following Section 3.2.) because the closest SrCoO_{2.5} composition to our impurity is AFM with high Néel temperature $T_N = 570$ K [52]. Moreover, the less content of oxygen and cobalt, the much lower T_C compared with our

$T_C \approx 250$ K and much weaker FM interactions [8, 53-56]. The main lattice parameters are listed in Table 1 and are consistent with other literature data [24, 57]. With increasing t_{ann} , a unit cell volume V is increased non-monotonically, indicating the successive replacement of smaller La^{3+} cation ($r_{\text{La}^{3+}} = 0.136$ nm) by bigger Sr^{2+} cation ($r_{\text{Sr}^{2+}} = 0.144$ nm) in 12-fold oxygen coordination [58]. At the same time, the average size of coherent scattering regions D_{XRD} , determined *via* the Scherrer equation [59], increases with increasing t_{ann} from 48 nm for the LSCO-850 to 54 nm for the LSCO-875 and 60 nm for the LSCO-900 (Table 2 and ESI 1).

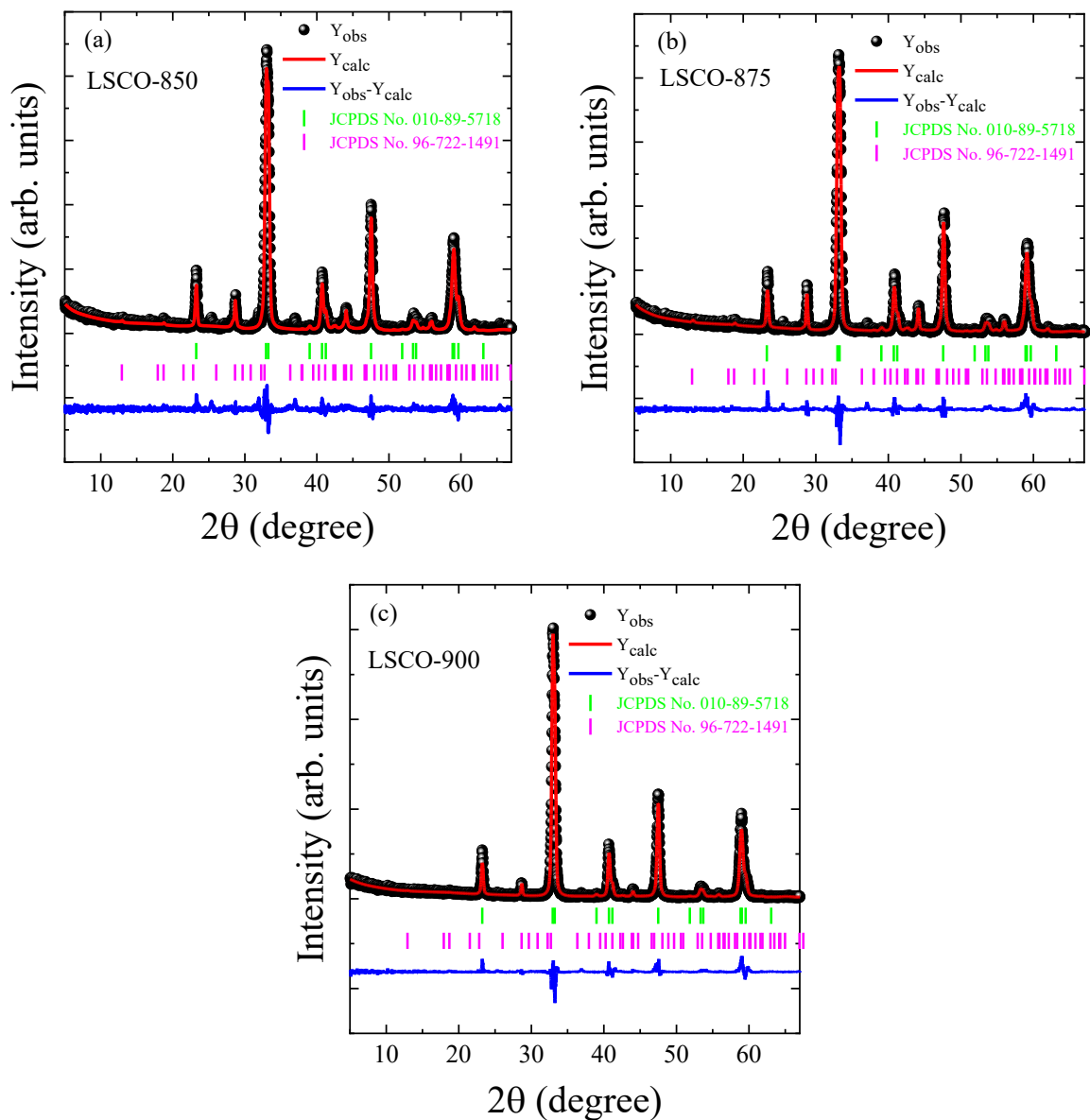


Fig. 1. XRD patterns of the LSCO measured at room temperature and fitted by the Rietveld method. The experimental (black cycles) and calculated (red up curve) values and a difference curve (blue bottom line) normalized to a statistical error are presented. Vertical bars are the calculated positions of diffraction peaks corresponding to the main rhombohedral $R\bar{3}c$ perovskite structure and rhombohedral $R32$ impurity $\text{SrCo}_{0.78}\text{O}_{2.48}$ in the LSCO-850, LSCO-875, and LSCO-900.

Table 1

Rietveld refinement crystallographic parameters of the LSCO nanopowders at different t_{ann}						
t_{ann} (°C)	850		875		900	
Phase composition	La _{0.6} Sr _{0.4} CoO ₃ 82.6%	SrCo _{0.78} O _{2.48} 17.4%	La _{0.6} Sr _{0.4} CoO ₃ 85.2%	SrCo _{0.78} O _{2.48} 14.8%	La _{0.6} Sr _{0.4} CoO ₃ 92.0%	SrCo _{0.78} O _{2.48} 8.0%
Space group	$R\bar{3}c$ (No. 167)	$R32$ (No. 155)	$R\bar{3}c$ (No. 167)	$R32$ (No. 155)	$R\bar{3}c$ (No. 167)	$R32$ (No. 155)
a (Å)	5.43171(24)	9.46930(176)	5.42651(22)	9.46644(123)	5.43219(17)	9.47809(280)
b (Å)	5.43171(24)	9.46930(176)	5.42651(22)	9.46644(123)	5.43219(17)	9.47809(280)
c (Å)	13.12327(97)	12.39900(378)	13.12711(86)	12.36905(277)	13.14732(83)	12.37605(411)
V (Å ³)	335.310(32)	962.837(387)	334.766(29)	959.931(278)	335.984(26)	962.840(514)
Z	6	18	6	18	6	18
ρ (g/cm ³)	6.695	5.379	6.708	5.395	6.676	5.379
R_p (%)		10.9		10.4		10.3
R_{wp} (%)		15.2		14.1		13.6
R_{exp} (%)		9.76		10.05		9.94
χ^2 (%)		2.43		1.98		1.87

The morphology and particle size distribution of the LSCO were studied using SEM and TEM data (see Figs. 2 and 3). All LSCO nanopowders demonstrate well-developed structural nature with a spherical-like shape of nanoparticles. An average particle size D and their distribution (see Table 2) were defined using a detailed approach described in our previous work [45]. With increasing t_{ann} , the particle size is increased from $D_{SEM} = 74$ nm and $D_{TEM} = 39$ nm for the LSCO-850 to 75 and 44 nm for the LSCO-875 and 79 and 47 nm for the LSCO-900, which correlates with the XRD data. The differences between SEM and TEM data may be associated with insufficient datasets by size. It should be noted that a dispersion σ is relatively high, indicating the existence of particles with a big difference in their sizes. Additionally, the chemical composition of all LSCO is approximately confirmed as 0.6:0.4:1 according to the EDS data (see Fig. 2 (b, d, f)).

Table 2

Particle size distribution based on the XRD, SEM, and TEM data for LSCO at different t_{ann}										
t_{ann} (°C)	XRD		SEM			TEM				
	D_{XRD} (nm)	D_{SEM} (nm)	Function	σ	R^2	D_{TEM} (nm)	Function	σ	R^2	
850	48±1	74±3	Lorentz	28±9	0.62297	39±2	LogNormal	32±6	0.87573	
875	54±1	75±2	Gaussian	54±5	0.96482	44±1	LogNormal	28±2	0.98392	
900	60±1	79±1	Gaussian	63±3	0.98155	47±1	LogNormal	13±2	0.97304	

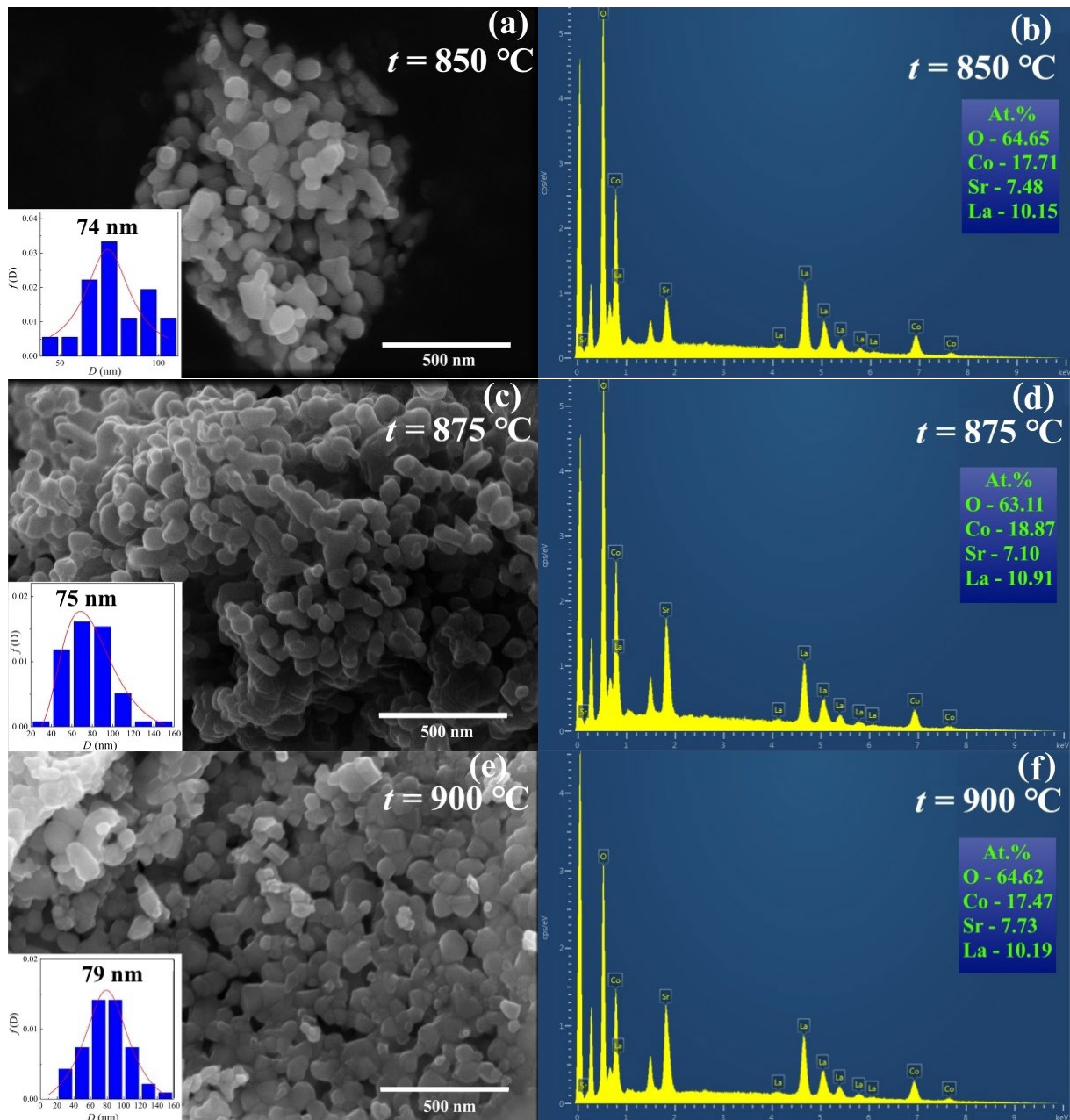


Fig. 2. SEM and EDS images of the LSCO compositions obtained at $t_{\text{ann}} = 850$ (a, b), 875 (c, d), and $900\text{ }^{\circ}\text{C}$ (e, f). Insets show particles' distribution with an average particle size D_{SEM} .

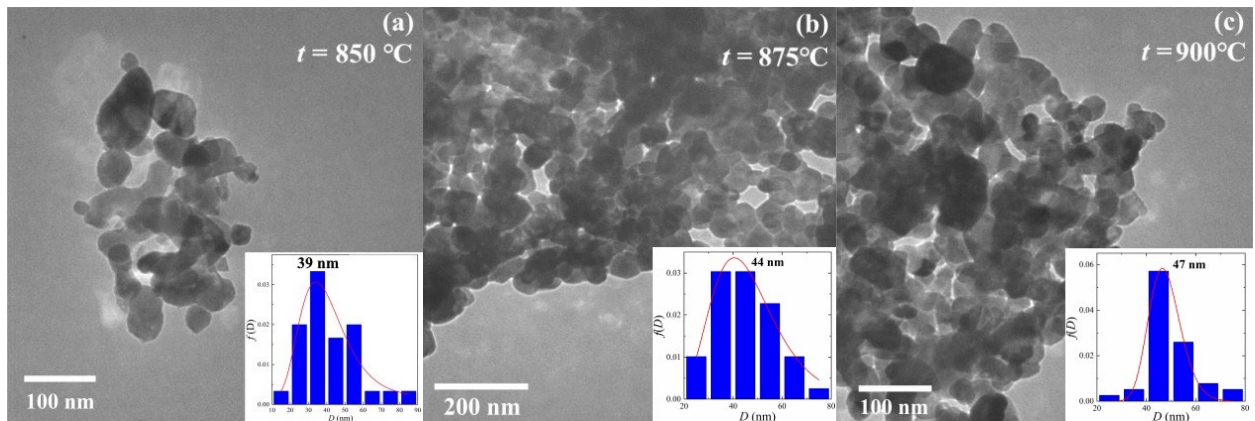


Fig. 3. TEM images of the LSCO nanopowders obtained at $t_{\text{ann}} = 850$ (a), 875 (b), and $900\text{ }^{\circ}\text{C}$ (c). Insets show particles' distribution with an average particle size D_{TEM} .

3.2. Magnetic properties

The field dependences of magnetization $M(H)$ for the LSCO-900 at 2, 77, and 300 K are presented in Fig. 4. The LSCO-900 is in FM at 2 and 77 K and PM at 300 K states. At 2 K, the spontaneous magnetization M_S achieves 10.5 emu/g, and there is no saturation even under magnetic field 3 T that indicates competing between FM DE $\text{Co}^{3+}\text{--Co}^{4+}$ and AFM superexchange $\text{Co}^{3+}\text{--Co}^{3+}$ and $\text{Co}^{4+}\text{--Co}^{4+}$ interactions [60]. At the same time, Co ions can be in high-spin (HS), low-spin (LS), and/or even intermediate-spin (IS) states [12]. Based on the experimentally defined FM moment $\mu_{\text{FM}}^{\text{exp}} = 0.42\mu_{\text{B}}$ and other data [6, 7, 11, 53], it can be concluded that the most probable spin state for Co^{3+} and Co^{4+} ions are HS ($t_{2g}^4e_g^2$) with $S = 4/2$ and LS ($t_{2g}^5e_g^0$) with $S = 1/2$ states, respectively. Theoretical calculation gives $\mu_{\text{FM}}^{\text{theor}} = 2.8\mu_{\text{B}}$. The big difference between theoretical and experimental data may be associated with competing for different magnetic interactions and the presence of oxygen vacancies [7, 50, 61, 62]. The main magnetic parameters are listed in Table 3. It should be noted that the LSCO-900 is a ferromagnet with a strong coercivity $H_C = 4.3$ kOe and residual magnetization $M_r = 7.2$ emu/g at 2 K (see the inset of Fig. 4).

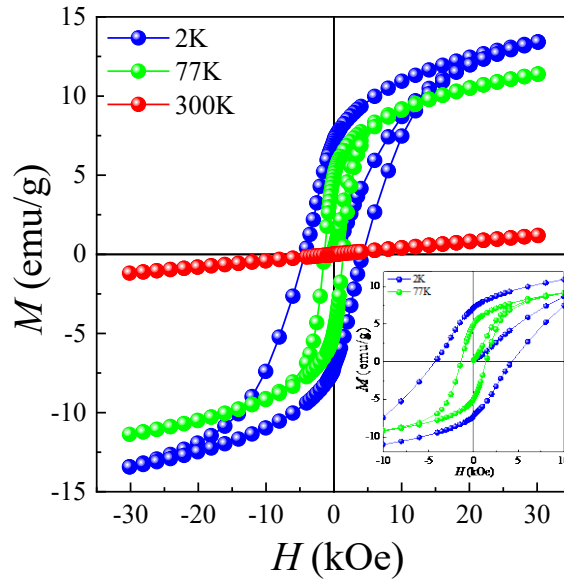


Fig. 4. Field dependences of magnetization $M(H)$ at 2, 77, and 300 K for the LSCO-900. The inset shows an enlarged area of the $M(H)$.

Table 3

The main magnetic parameters: spontaneous magnetization M_S , residual magnetization M_r , coercivity H_C , characteristic Curie temperatures T_{C1} , T_{C2} , T_{C3} , T_{C4} , AFM transition temperature T_t , and blocking temperature T_B under different pressures P for the LSCO-900

P (GPa)	FM						Near phase transitions					
	M_S (emu/g)		M_r (emu/g)		H_C (kOe)		FC	ZFC	FC	ZFC	ZFC	ZFC
	2 (K)	77 (K)	2 (K)	77 (K)	2 (K)	77 (K)	T_{C1} (K)	T_{C2} (K)	T_{C3} (K)	T_{C4} (K)	T_{AFM} (K)	T_B (K)
0	10.5	8.7	7.2	4.9	4.3	1.4	251	255	163	187	145	169
0.16	–	–	–	–	–	–	259	261	161	186	150	164
0.43	–	–	–	–	–	–	260	263	162	190	153	168
0.64	–	–	–	–	–	–	265	267	165	191	156	170
0.76	–	–	–	–	–	–	266	269	166	194	158	170

The temperature dependences of magnetization $M_{ZFC}(T)$ and $M_{FC}(T)$ for the LSCO-900 under different pressures P and in the magnetic field $H = 50$ Oe (Fig. 5) correspond to a typical behavior of the nanoparticles with FM and AFM inclusions, as well as with randomly oriented uniaxial magnetic anisotropy [63, 64]. From the temperature dependences of the extremum of the derivative of the magnetic susceptibility $d(M/H)/dT$, where $\chi = M/H$ (see the insets in Fig. 5), several characteristic phase transition temperatures were determined (Table 3). Noteworthy, four characteristic Curie temperatures $T_{C1} = 251$ K and $T_{C3} = 163$ K from FC and $T_{C2} = 255$ K and $T_{C4} = 187$ K from ZFC curves were defined as an example for the LSCO-900 without pressure $P = 0$ (see the insets in Fig. 5). The observed difference between ZFC and FC Curie temperatures is associated with "pinning" magnetic moments on the magnetic inhomogeneities and structural defects, as well as the competing different magnetic exchange interactions [18, 46, 61, 65]. The obtained average ZFC and FC Curie temperatures 175 and 253 K indicate the presence of smaller and bigger nanoparticles in the LSCO-900 [45, 66]. The highest Curie temperature, 253 K ($P = 0$), is compliant with other literature data 230 K [11] and 246 K [7] for the same ceramic bulk composition. An additional contribution to the ZFC and FC curves at $T < 187$ K is due to the magnetization from smaller particles. As shown [45, 66], a change in the Curie temperature T_C value is caused by the particle size distribution. It means that in our case, the change of the average Curie temperatures in ~ 1.4 times corresponds to the existence of bigger $D_{XRD} \approx 60$ nm (see Table 2) with $T_C = 253$ K and smaller $D_{XRD} \approx 43$ nm with $T_C = 175$ K nanoparticles. Moreover, the blocking temperature $T_B = 169$ K, determined from the maximum temperature on the $M_{ZFC}(T)$ curve, is observed for the LSCO-900 ($P = 0$). At $T < T_B$, the magnetic nanoparticles are in a

blocked state. At $T_B \leq T \leq T_{C2}$, the thermal fluctuations of the magnetization exceed the difference of the spin states between two energy minima, and the magnetic nanoparticles are in an unblocked state. At $T > T_{C2}$, the magnetic nanoparticles pass into the PM state. Additionally, an abnormal decreasing magnetization $M_{ZFC}(T)$ at an AFM transition temperature T_{AFM} is observed (Fig. 5(b)) that is caused by AFM contribution of nanoparticles' "dead" skin [67].

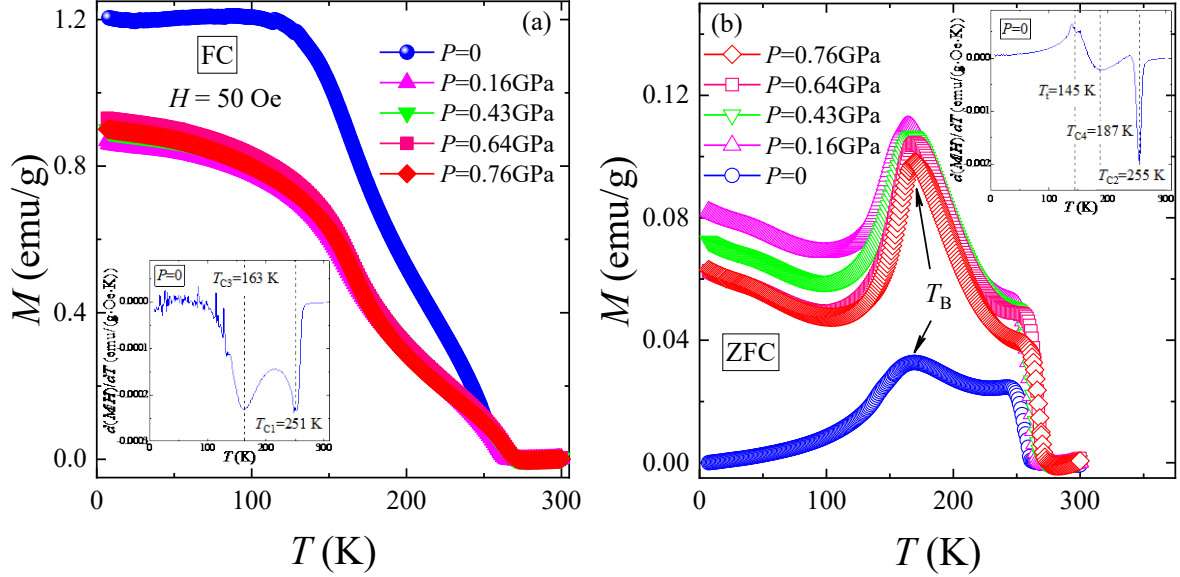


Fig. 5. Temperature dependences of the magnetization $M_{FC}(T)$ (a) and $M_{ZFC}(T)$ (b) for the LSCO-900 under different pressures P and in the field of $H = 50$ Oe. The insets show the defined characteristic Curie temperatures T_{C1} and T_{C3} (a) and T_{C2} and T_{C4} (b), as well as AFM transition temperature T_{AFM} and blocking temperature T_B (b).

As pressure P increases, the FM and AFM subsystems become more magnetically homogeneous. The characteristic Curie temperatures T_{C1} and T_{C2} for bigger and T_{C3} and T_{C4} for smaller nanoparticles increase with a pressure rise (Table 3), indicating the strengthening of the FM DE $\text{Co}^{3+}-\text{O}^{2-}-\text{Co}^{4+}$. At the same time, the T_{AFM} also increases, demonstrating the improvement of the AFM superexchanges $\text{Co}^{3+}-\text{O}^{2-}-\text{Co}^{3+}$ and $\text{Co}^{4+}-\text{O}^{2-}-\text{Co}^{4+}$, whereas the blocking temperature T_B increases slightly (Table 3). The characteristic Curie temperatures show a linear-like behavior *versus* pressure (Fig. 6). This allows us to define an average $\langle dT_C/dP \rangle$ ratio for smaller and bigger nanoparticles being 10 and 13 K/GPa, respectively. The obtained values show that bigger nanoparticles are more sensitive to the external pressure P , and their magnetic parameters can be easily controlled.

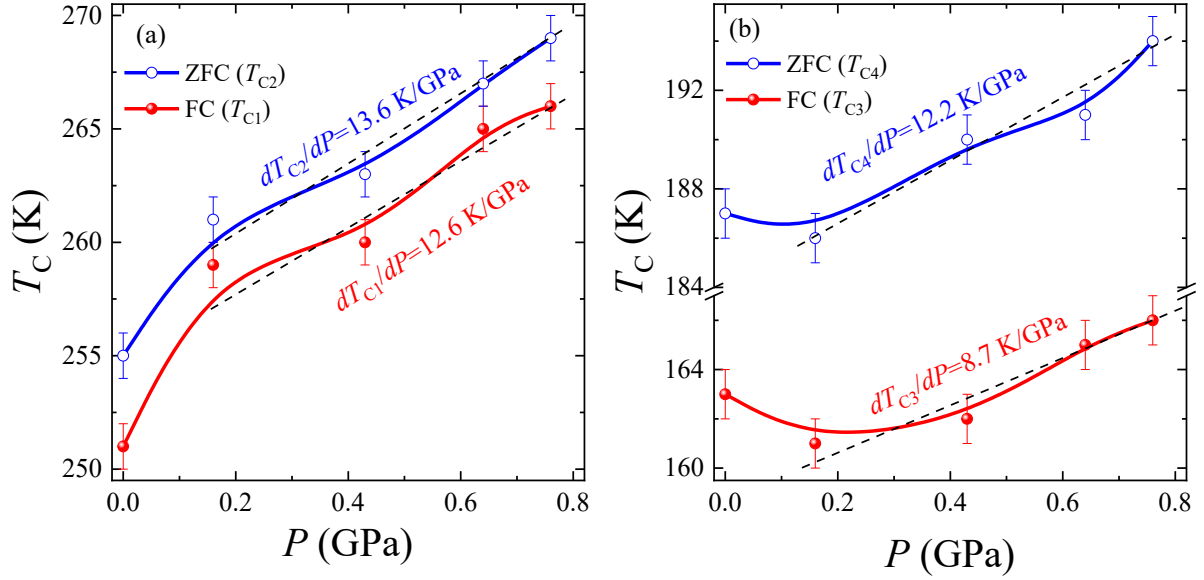


Fig. 6. Pressure dependences of characteristic Curie temperatures T_{C1} and T_{C2} (a) and T_{C3} and T_{C4} (b) defined from the ZFC-FC curves for the LSCO-900. The dashed lines show linear behavior T_C versus P .

The isothermal magnetization curves $M(H)$ around T_C in a wide temperature range from 200 to 300 K with a $\Delta T = 2$ K step for the LSCO-900 are shown in Fig. 7(a). At $T > T_C$, the magnetization increases linearly with an applied magnetic field, indicating the PM state of the sample. At $T < T_C$, the linear isothermal magnetization behavior turns to a curve, which indicates passing to the FM state. At the same time, the magnetization cannot be saturated even at lower temperatures and higher magnetic fields, probably because of AFM phase contribution^[68]. According to the Banerjee criterion,^[69] the positive slope of Arrott's curves $M^2(H/M)$ (see Fig. 7(b)) near the Curie temperature is observed, which indicates a second-order magnetic phase transition for the LSCO-900.

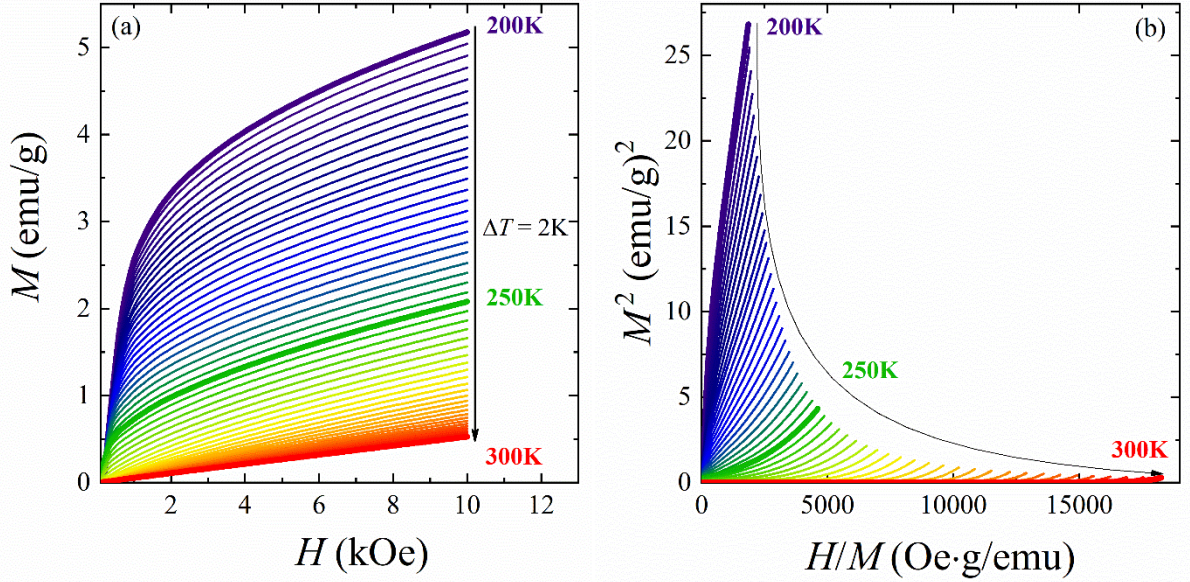


Fig. 7. Isotherms of magnetization $M(H)$ (a) and Arrott's plots $M^2(H/M)$ (b) within 200–300 K with a $\Delta T = 2$ K step for the LSCO-900.

The temperature dependences of the magnetic entropy change $-\Delta S_M(T, H)$ near phase transition(s) (Fig. 8) were plotted using the isotherms of magnetization $M(H)$ and the numerical integration method of the Maxwell relation ^[70]:

$$\Delta S_M(T, \mu_0 H) = S_M(T, \mu_0 H) - S_M(T, 0) = \int_0^{\mu_0 H} (\partial M / \partial T)_{\mu_0 H} d(\mu_0 H). \quad (1)$$

The magnetic entropy change $-\Delta S_M(T, H)$ shows a vast indistinct peak with relatively low values of MCE. Upon application of the external high hydrostatic pressure $P \approx 0.8$ GPa and with increasing the magnetic field ΔH up to 10 kOe, the MCE peak position moves towards higher temperatures from 250 to 256 K, indicating the domination of the FM DE over AFM superexchange interactions, whereas without pressure $P = 0$ we have opposite situation and reducing from 247 to 233 K (Fig. 8). Moreover, the δT_{FWHM} for the $-\Delta S_M^{\max}$ is far more than 50 K that makes the studied LSCO-900 is a promising component for creating the magnetic refrigerant composites working a wide temperature range.

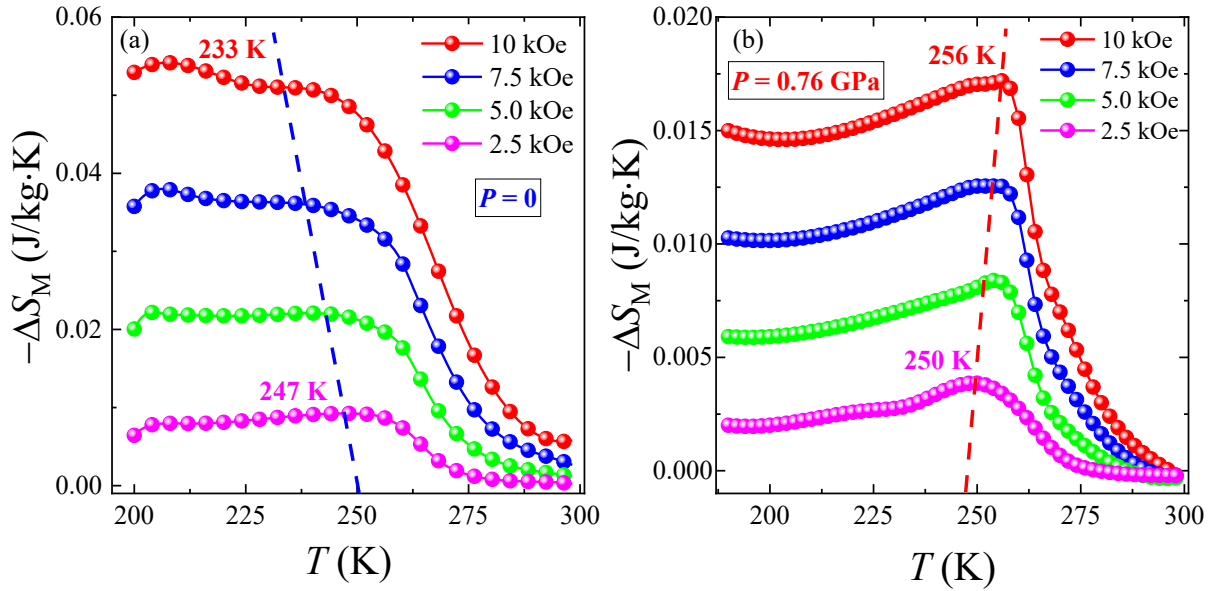


Fig. 8. Temperature dependences of magnetic entropy change $-\Delta S_M(T)$ without pressure $P = 0$ (a) and under high-pressure $P \approx 0.8$ GPa (b) in the magnetic field ΔH up to 10 kOe for the LSCO-900.

3.3. Electrocatalytic properties

As mentioned in the introduction, interest in Ln- and Co-containing perovskites as electrocatalysts for OER in an alkaline environment has increased significantly recently [28, 30-36, 41-44]. In order to find out the OER activity for water splitting of the prepared LSCO samples, electrochemical tests were carried out in 1M KOH electrolyte (pH = 14) with the following sequence: multiple current-voltage (CV) scans (until stable electrode operation is achieved), alternative current (AC) impedance, recording of LSV curves with iR correction, long-term chronopotentiometry tests (at a current density of $10 \text{ mA}\cdot\text{cm}^{-2}$) and re-registration of LSV curves. It should be emphasized that Co- and Ni-containing complex oxides can be entirely or partially *in situ* transformed into oxides/hydroxides due to electrochemical processes in an alkaline medium [71, 72]. Accordingly, after a long electrochemical treatment, we investigated the electrode materials to verify the stability of the LSCO catalysts.

Before the electrochemical test, the manufactured electrodes were placed in an electrolyte environment for 1 h to establish equilibrium at the electrode-electrolyte interface. As shown in Fig. S2, for all samples, the shape of the CV curves in the range of 0.9–1.8 V is similar at the corresponding scanning rate (from 1 to $50 \text{ mV}\cdot\text{s}^{-1}$). Only the peak around 1.3 V (anodic scans) is clearly observed,

corresponding to the $\text{Co}^{4+} \rightarrow \text{Co}^{3+}$ transformation [47]. As AC impedance measurements show (Fig. 9(a)), the LSCO-900 sample has the best conductivity. Nyquist plots correspond to the equivalent circuit, which includes series resistance R_s , the EDLC at the active material/electrolyte interface C_{dl} , electron transfer resistance R_{ct} , and the diffusion impedance Warburg impedance (Fig. S3). The impedance spectra include two parts, a line in a low-frequency region and a semicircle in a high-frequency region. The numerical value of the diameter of the semicircle on the Z_0 axis is approximately equal to the charge transfer resistance R_{ct} , and the sloping line corresponds to the Warburg impedance, which is associated with electrolyte diffusion in electrode materials. As known, the Helmholtz double layer capacitance C_{dl} appears due to the porosity of the active material and the uneven distribution of the current on the electrode surface [73]. The double-layer capacitance C_{dl} was measured by cyclic voltammetry for determined the electrochemically active surface area (ECSA) (see details in ESI2). Fig. S4 shows CV curves recorded in the potential windows from 0 to 0.1 V vs. Hg/HgO at a scan rate of 1–10 $\text{mV}\cdot\text{s}^{-1}$. It is known that the ECSA value corresponds to the number of potential active sites for electrocatalysis, and R_{ct} is inversely proportional to electrochemical activity. In this way, the calculated values ESCA for the LSCO-800, LSCO-850, and LSCO-900 were 15.97 cm^2 , 17.26 cm^2 , and 24.53 cm^2 , respectively, whereas the resistance values R_{ct} were 1.05, 0.9, and 0.6 Ohm. Thereby, a low charge transfer resistance and high ESCA indicate good electronic conductivity and a high rate of OH ion transfer across the boundaries between the electrolyte and active electrode materials. The above AC impedance results show that the LSCO-900 has the attributes of an efficient electrocatalyst for OER in an alkaline environment.

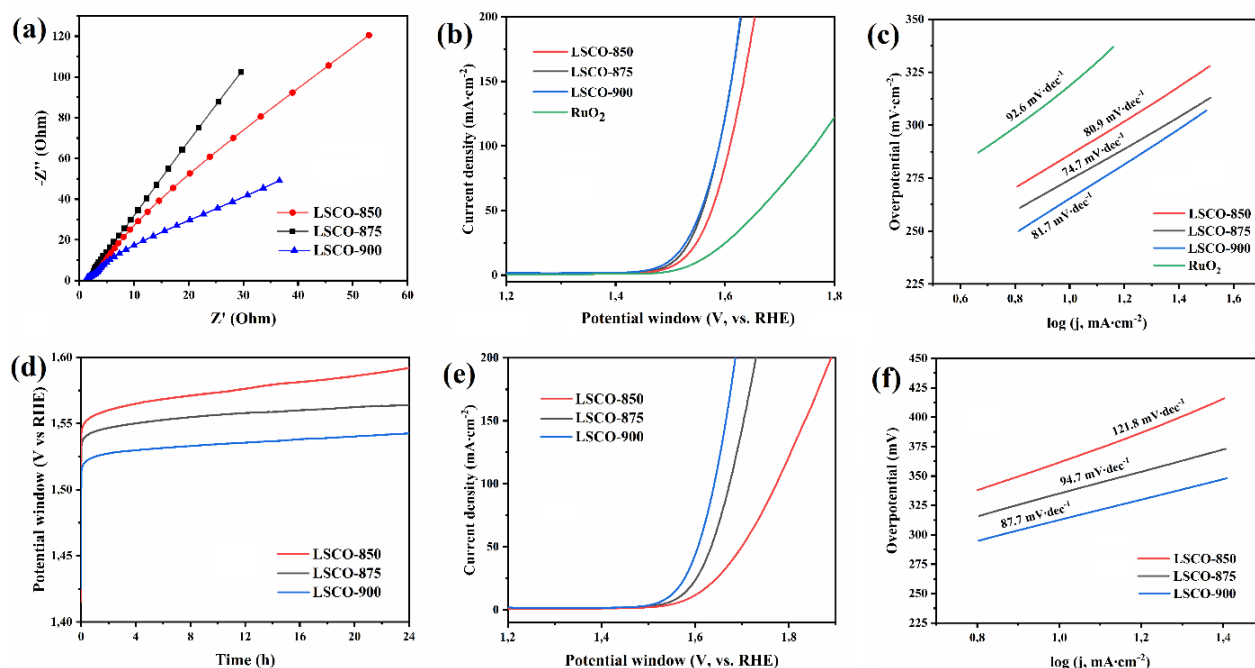


Fig. 9. Electrochemical testing for the LSCO electrodes in 1 M KOH: (a) Nyquist plots; (b) and (c) LSV curves and Tafel plots before the long-term stability test for the LSCO catalysts and RuO₂ at a scan rate of 1 mV s⁻¹ (iR-compensation 90%); (d) time dependence of potential under a constant current density of 10 mA cm⁻²; (e) and (f) LSV curves and Tafel plots after the long-term stability test at a scan rate of 1 mV s⁻¹.

According to onset LSV measurements, all LSCO samples exhibited highly efficient electrocatalytic activity for alkaline OER and a slow boost of current density with the increase of applied potential (Fig. 9(b)). The obtained overpotentials values' intervals were only 265–285 mV and 360–380 mV when reaching a current density of 10 and 100 mA cm⁻², respectively (more details are given in Table S2). The LSV curves for the LSCO-900 and LSCO-875 electrodes are almost identical, and the overpotential OER for the LSCO-850 is slightly higher. It is important that the commercial electrocatalyst of noble metal oxide (RuO₂) used for comparison showed worse activity. These results confirm the calculations of the Tafel slope (Fig. 9(c)): for the synthesized LSCO samples, the range of values is 74–82 mV·dec⁻¹, and for commercial RuO₂ is slightly more than 92 mV·dec⁻¹. The subsequent long-term test of electrodes during continuous electrolysis (current density 10 mA·cm⁻²) is presented in Fig. 9(d). The continuous formation of oxygen bubbles on the surface of the electrodes was observed when the stability tests were carried out. For all samples, an increase in overpotential OER is observed during the first 4 h of the chronopotentiometry test, and the values of η_{10} reach 300, 320, and 335 mV for the LSCO-900, LSCO-875, and LSCO-850,

respectively. However, the activity of the electrocatalysts decays much more slowly during the next 20 h of electrolysis, especially in the case of the LSCO-900 sample (the magnitude of the overpotential increases by only 12 mV); more detailed these results for all electrodes presented in Table S3. The slight increase in voltage after 4 h of the test proves the final stabilization of all electrodes and the high efficiency of the LSCO materials as OER catalysts. It should also be considered that carbon fiber (the base of the electrode used in this study) is gradually destroyed in an alkaline environment under OER conditions ^[72]. This leads to breakdowns of the interface between the catalyst and the collector-electrode and is an additional factor in the growth of overpotential OER during long-term tests. LSV curves measured after long-term stability tests (Fig. 9(e)) are in good agreement with CP results: the values of overpotential η_{10} for the corresponding samples are identical (Tables S2 and S3). Re-registration LSV measurements revealed that in the range of current densities from 10 to 100, the OER overvoltage increased by only 14–17% for the LSCO-900 electrode, while for the LSCO-875 and LSCO-850, the changes were 22–24 and 27–44%, respectively (Table S2). Calculation of the Tafel slope after long-term electrolysis (Fig. 9(f)) also indicates the preservation of high catalytic activity of the LSCO-900 material, in contrast to the LSCO-875 and especially LSCO-850 samples.

Electrode materials were also studied in detail after CP tests. According to the XRD, all LSCO samples retained their crystallinity. As shown in Fig. S5, the diffraction patterns show reflections from both crystalline phases ($\text{La}_{0.6}\text{Sr}_{0.4}\text{CoO}_3$ and $\text{SrCo}_{0.78}\text{O}_{2.48}$). This proves the high stability of Ln and Co-containing complex oxides in an alkaline environment during long-term electrolysis, in contrast to similar Mn-containing compounds ^[45]. SEM and elemental mapping of the electrode surface after prolonged electrolysis mostly support this conclusion (Fig. S6–S8). The SEM images mostly show nanoparticles as in the initial LSCO material, which agrees with the elemental mapping. However, a careful analysis of the images revealed that the formation of nanoflakes is observed in some areas (Fig. S7). In addition, the XPS study was performed before and after the electrochemical tests to elucidate the features of possible transformations on the surface of the LSCO for the electrode

with the best catalytic performance (LSCO-900). In both cases, the survey spectra of the LSCO-900 electrode show the existence of La, Sr, Co, O, and C peaks (Fig. S9). As expected, La and Sr ions are trivalent and divalent before and after electrocatalysis (Fig. S9 and Table S4).

Nevertheless, the high-resolution XPS spectra revealed some differences (a detailed description is provided in the ESI3). Changes are also observed for the HR-XPS spectra of Co2p (Fig. 10): exhibit two prominent peaks at around 780.1 and 795.6 eV for the electrode before and at around 778.8 and 794 eV after electrocatalysis, which correspond to the Co2p_{3/2} and Co2p_{1/2} states, respectively. Both Co2p spectra were decomposed into two components (Fig. 10(b, c)), suggesting cobalt ions' presence in Co³⁺ and Co⁴⁺ oxidation states. The positions of their peak centers are listed in Table S5 (ESI3) and are in good agreement with other literature XPS data [16, 74, 75]. The determined values of the Co³⁺/Co⁴⁺ ratio differ before 52.4/47.6 and after 61.8/38.2 electrocatalysis. It indicates the growth of the Co³⁺ content and is only a quality picture of the cobalt ions content due to the presence of additional weak Co²⁺ at around 786 eV and Co₃O₄ at around 790 eV satellite peaks [76]. In support of the Co³⁺ content growth, the following factors should be noted. First, the LSCO-900 spectrum after electrocatalysis is slightly shifted towards the lower energy ~ 1.3 eV relative to the one before electrocatalysis, indicating an increase of the Co³⁺ concentration. Second, the simultaneous reducing Co²⁺ satellite peak and, as a result, its content and increasing Co₃O₄ satellite peak, consisting of the mixed Co²⁺ and Co³⁺ states, is observed for the sample after electrocatalysis. Third, the full-width at half-maximum (FWHM) of the Co2p_{3/2} main peak decreases ~ 2.0 eV after electrocatalysis, suggesting more Co³⁺ and fewer Co²⁺ ions on the surface [77]. Therefore, the XPS study clearly indicates significant changes in the surface layer of the LSCO catalyst after long-term electrolysis in an alkaline environment. Because the crystallinity and morphology of the original LSCO material remain intact, the formation of a dense amorphized layer with high catalytic activity on the surface of the LSCO should be assumed, essentially the formation of a core-shell structure.

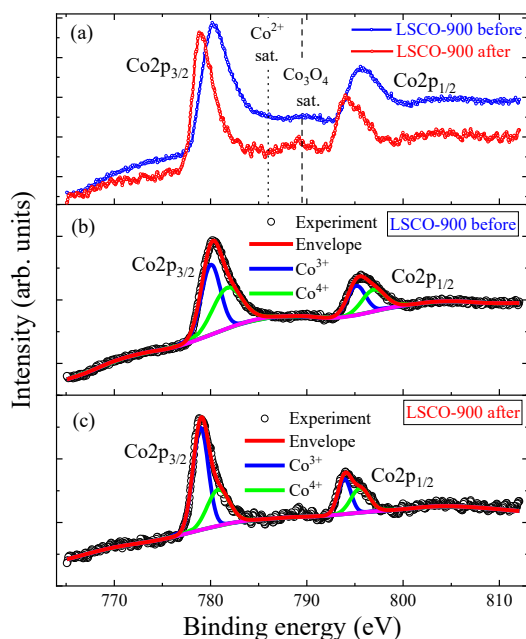


Fig. 10. Co2p spectra (cycles) for the LSCO-900 before and after electrocatalysis (a), as well as their fitting by red envelope line and decomposition into Co^{3+} (blue line) and Co^{4+} (green line) components with a baseline (magenta line) in the LSCO-900 before (b) and after (c) electrocatalysis. The dashed and dotted lines indicate the energy position of the Co_3O_4 and Co^{2+} satellite peaks, respectively.

Table 4 lists the comparative characteristics of OER for electrocatalysts based on La, Co-containing perovskites in an alkaline electrolyte. Among them, the LSCO material described here occupies a leading position. It should be noted that very recently, it was reported that the amorphization of crystallized nanometer perovskite LaCoO_3 to a highly disordered state leads to improved electrocatalytic properties of OER [44]. In our case, a highly active amorphized layer is formed on the surface of the LSCO nanoparticles during electrolysis. The catalytic activity increases with increasing the proportion of this crystalline phase for a number of the LSCO-850, LSCO-875, and LSCO-900 samples. In addition, the high stability of the amorphized layer prevents further destruction of the nanoparticles and protection of the initial morphology, which can provide a significant electroactive surface area for a long time. Finally, forming *in situ* core-shell nanostructures based on perovskites is a potentially successful strategy for creating highly active and stable electrocatalysts.

Table 4**Comparison of OER properties for LaCo-based electrocatalysts in alkaline electrolyte.**

Catalyst	Electrolyte	η_{10} (mV)	Tafel slope	Ref.
LSCO-900	1M KOH	265	81.7	This work
		312*	87.7*	
LSCO-850	1M KOH	275	74.7	This work
		335*	94.7*	
LSCO-875	1M KOH	285	80.9	This work
		362*	121.8*	
LaCoO ₃ -Reduce	1M KOH	293	63.4	[44]
La _{0.5} Pr _{0.5} CoO ₃	1M KOH	312	80.6	[28]
La(Co _{0.71} Ni _{0.25}) _{0.96} O ₃	0.1M KOH	324	71	[29]
La(CrMnFeCo ₂ Ni)O ₃	1M KOH	325	51.2	[30]
La _{0.7} Sr _{0.3} CoO _{3-P}	1M KOH	326	70.8	[31]
Cl-LaCoO ₃	1M KOH	342	76.2	[42]
(La _{0.776} Sr _{0.224}) _{0.9} (Co _{0.087} Fe _{0.84} Ru _{0.073}) _{1.026} O _{3-δ}	1M KOH	347	54.7	[32]
La-CoO _x	0.1M KOH	353	78.2	[41]
La _{0.4} Sr _{0.6} Co _{0.7} Fe _{0.2} Nb _{0.1} O _{3-δ}	0.1M KOH	360	78	[33]
La _{0.9} CoO _{3-δ}	0.1M KOH	380	82.5	[78]
La _{0.96} Ce _{0.04} CoO ₃	1M KOH	380	80	[34]
La _{0.6} Sr _{0.4} Co _{0.8} Fe _{0.2} O ₃	0.1M KOH	385	76.7	[35]
LaCoO ₃	0.5M KOH	396	144.8	[79]
Pt/LaCoO ₃	1M KOH	327	92	[43]
LaMn _{0.4} Co _{0.6} O ₃	1M KOH	400	95	[36]
La _{0.699} Sr _{0.301} Co _{0.702} Fe _{0.298} O _{2.92}	1M KOH	440	109	[37]
LaCoO ₃	0.1M KOH	490	69	[39]

*After 24 h of incessant electrolysis (current density 10 mA·cm⁻²).

4. Conclusions

The structure, morphology, particle size distribution, and magnetic phase transitions, as well as magnetic, magnetocaloric, and electrochemical properties of the LSCO nanopowders obtained under different annealing temperatures $t_{\text{ann}} = 850, 875, \text{ and } 900$ °C have been studied comprehensively. All samples indicate the rhombohedral $R\bar{3}c$ perovskite structure, improving its single-phase nature with increasing t_{ann} . At the same time, it leads to increasing unit cell volume V , an average particle size D , and its dispersion σ . The LSCO-900 composition mainly consists of the Co³⁺ and Co⁴⁺ ions, as well as minor Co²⁺ and Co₃O₄ traces that play a crucial role in forming magnetic and electrochemical properties. The main magnetic parameters such as spontaneous magnetization M_S , coercivity H_C , residual magnetization M_r , phase transition temperatures, and magnetic entropy change $-\Delta S_M$ have been defined. The LSCO-900 sample is a ferromagnet with a high $H_C = 4.3$ kOe. It has been found that the LSCO-900 exhibits two characteristic Curie

temperatures, T_{C1} and T_{C2} , which are associated with the presence of nanoparticles of different sizes. Additionally, FM and AFM subsystems are stabilized and become more magnetically homogeneous because of applied external hydrostatic high-pressure P . As pressure increases, the average $\langle T_{C1} \rangle$ and $\langle T_{C2} \rangle$ increase from 253 and 175 K under ambient pressure to 268 and 180 K under $P \approx 0.8$ GPa, respectively. At the same time, the AFM transition temperature T_{AFM} and blocking temperature T_B also increase from 145 and 169 K to 158 and 170 K, respectively. The rise of $\langle dT_{C1}/dP \rangle$ for bigger particles and $\langle dT_{C2}/dP \rangle$ for smaller particles differs and is 13 and 10 K/GPa, respectively. The MCE in the LSCO-900 nanopowder is near the Curie temperature and has a second-order phase transition. The values of $-\Delta S_M$ are quite low and equals 0.05 J/kg·K without pressure and 0.017 J/kg·K under $P \approx 0.8$ GPa in the magnetic field 1 T, but with extremely wide peak $\delta T_{FWHM} > 50$ K.

The obtained series of the LSCO nanomaterials showed excellent characteristics as electrocatalysts for overall water splitting (OER process) in 1 M KOH electrolyte. The values of the initial overpotential of oxygen generation were within 265–285 mV (a current density of 10 mA/cm²), and the sample with the highest content of the La_{0.6}Sr_{0.4}CoO₃ phase showed the best performance. The LSCO materials described here retain high catalytic activity during long-term electrolysis, which should be attributed to the formation of a stable amorphization layer on the surface of nanoparticles. Accordingly, a significant area of the catalytically active surface, resulting from the emergence of stable core-shell nanosystems, can ensure high efficiency of practical use of the material.

The parallel study of nanopowders' physical and electrocatalytic properties in this work made it possible to establish the physical and chemical basis of the various samples obtained at different t_{ann} and find ways to obtain materials for practical application in electrocatalysis. The research of magnetic and magnetocaloric properties of the samples opens up the possibility of changing the conditions of catalysis by changing the temperature of the electrocatalyst by a contactless method using an electromagnetic field. The obtained results demonstrate a simple way to improve complex oxides with a perovskite structure for various functional purposes.

Author Contributions

Han Lin: Writing - original draft, Data curation, Investigation, Methodology. N.A. Liedienov: Writing - review & editing, Conceptualization, Data curation, Investigation. I.V. Zatovsky: Writing - review & editing, Data curation, Conceptualization, Investigation. D.S. Butenko: Writing - review & editing, Data curation, Investigation, Methodology. I.V. Fesych: Data curation, Investigation, Methodology. Wei Xu: Data curation, Investigation, Methodology. Songchun Rui: Data curation, Investigation, Methodology. Quanjun Li: Data curation, Investigation, Methodology. Bingbing Liu: Data curation, Investigation, Methodology. A.V. Pashchenko: Data curation, Methodology. G.G. Levchenko: Writing - review & editing, Supervision.

Conflicts of interest

There are no conflicts to declare.

Acknowledgments

This research was financially sponsored by the European Federation of Academies of Sciences and Humanities within the framework of the "European Fund for Displaced Scientists" (Grant reference number EFDS-FL2-05). It was also supported by the Major Science and Technology Infrastructure Project of Material Genome Big-science Facilities Platform supported by the Municipal Development and Reform Commission of Shenzhen.

References

- [1] M. Chennabasappa, E. Petit, O. Toulemonde, Toward oxygen fully stoichiometric $\text{La}_{1-x}\text{Sr}_x\text{CoO}_3$ ($0.5 \leq x \leq 0.9$) perovskites: Itinerant magnetic mechanism more than double exchange one's, *Ceramics International* 46(5) (2020) 6067-6072.
- [2] N. Alhokbany, S. Almotairi, J. Ahmed, S.I. Al-Saeedi, T. Ahamad, S.M. Alshehri, Investigation of structural and electrical properties of synthesized Sr-doped lanthanum cobaltite ($\text{La}_{1-x}\text{Sr}_x\text{CoO}_3$) perovskite oxide, *Journal of King Saud University-Science* 33(4) (2021) 101419.
- [3] J. Qiang, D. Wang, S. Hui, Synthesis of $\text{La}_{1-x}\text{Sr}_x\text{CoO}_{3-\delta}$ and its REDOX performance in air, *Journal of Environmental Chemical Engineering* 10(6) (2022) 108794.
- [4] T.A. Ho, P.T. Long, N. Quang, S. Cho, S. Yu, Short and long range ordering in $\text{La}_{1-x}\text{Sr}_x\text{CoO}_3$ cobaltites, *Journal of Magnetism and Magnetic Materials* 477 (2019) 396-403.
- [5] E. Ahmed, H. Alamri, S. Elghnam, O. Eldarawi, T. Tawfik, A. Mahmoud, S. Elwan, Tuning Magnetocaloric Properties for $\text{La}_{1-x}\text{Sr}_x\text{CoO}_3$, *Physics of the Solid State* 63(11) (2021) 1601-1605.

- [6] V. Sikolenko, A. Sazonov, I. Troyanchuk, D. Töbrens, U. Zimmermann, E. Pomjakushina, H. Szymczak, Magnetic properties of $\text{La}_{1-x}\text{Sr}_x\text{CoO}_3$ ($x = 0.15$ and 0.3), *Journal of Physics: Condensed Matter* 16(41) (2004) 7313.
- [7] A. Petrov, O. Kononchuk, A. Andreev, V. Cherepanov, P. Kofstad, Crystal structure, electrical and magnetic properties of $\text{La}_{1-x}\text{Sr}_x\text{CoO}_{3-y}$, *Solid State Ionics* 80(3-4) (1995) 189-199.
- [8] M. Hoffmann, V.S. Borisov, S. Ostanin, I. Mertig, W. Hergert, A. Ernst, Magnetic properties of defect-free and oxygen-deficient cubic $\text{SrCoO}_{3-\delta}$, *Physical Review B* 92(9) (2015) 094427.
- [9] N. Loshkareva, E. Gan'shina, B. Belevtsev, Y.P. Sukhorukov, E. Mostovshchikova, A. Vinogradov, V. Krasovitsky, I. Chukanova, Optical, magneto-optical and transport properties of $\text{La}_{1-x}\text{Sr}_x\text{CoO}_3$ ($x = 0.15; 0.25; 0.35$) films: spin-state transition effects, *Journal of magnetism and magnetic materials* 258 (2003) 277-279.
- [10] J. Wu, C. Leighton, Glassy ferromagnetism and magnetic phase separation in $\text{La}_{1-x}\text{Sr}_x\text{CoO}_3$, *Physical Review B* 67(17) (2003) 174408.
- [11] Q. Xie, Z. Wu, X. Wu, W. Tan, Sr content on the structure and magnetic properties of $\text{La}_{1-x}\text{Sr}_x\text{CoO}_3$, *Journal of Alloys and Compounds* 474 (2009).
- [12] M. Senaris-Rodriguez, J. Goodenough, Magnetic and transport properties of the system $\text{La}_{1-x}\text{Sr}_x\text{CoO}_{3-\delta}$ ($0 < x < 0.50$), *Journal of Solid State Chemistry* 118(2) (1995).
- [13] M.G. Bellino, J.G. Sacanell, D.G. Lamas, A.G. Leyva, N.E. Walsöe de Reca, High-performance solid-oxide fuel cell cathodes based on cobaltite nanotubes, *Journal of the American Chemical Society* 129(11) (2007) 3066-3067.
- [14] R. Mahendiran, A. Raychaudhuri, Magnetoresistance of the spin-state-transition compound $\text{La}_{1-x}\text{Sr}_x\text{CoO}_3$, *Physical Review B* 54(22) (1996) 16044.
- [15] O. Gwon, S. Yoo, J. Shin, G. Kim, Optimization of $\text{La}_{1-x}\text{Sr}_x\text{CoO}_{3-\delta}$ perovskite cathodes for intermediate temperature solid oxide fuel cells through the analysis of crystal structure and electrical properties, *International journal of hydrogen energy* 39(35) (2014) 20806-20811.
- [16] Z. Cai, M. Kubicek, J.r. Fleig, B. Yildiz, Chemical Heterogeneities on $\text{La}_{0.6}\text{Sr}_{0.4}\text{CoO}_{3-\delta}$ Thin Films Correlations to Cathode Surface Activity and Stability, *Chemistry of materials* 24(6) (2012) 1116-1127.
- [17] A.J. Jacobson, Materials for solid oxide fuel cells, *Chemistry of Materials* 22(3) (2010) 660-674.
- [18] A. Pashchenko, N. Liedienov, V. Pashchenko, V. Prokopenko, V. Burhovetskii, A. Voznyak, I. Fesyeh, D. Tatarchuk, Y. Didenko, A. Gudymenko, Modification of multifunctional properties of the magnetoresistive $\text{La}_{0.6}\text{Sr}_{0.15}\text{Bi}_{0.15}\text{Mn}_{1.1-x}\text{B}_x\text{O}_{3-\delta}$ ceramics when replacing manganese with $3d$ -ions of Cr, Fe, Co, Ni, *Journal of Alloys and Compounds* 767 (2018) 1117-1125.
- [19] E.E. Ateia, A.T. Mohamed, M. Morsy, Humidity sensor applications based on mesopores LaCoO_3 , *Journal of Materials Science: Materials in Electronics* 30 (2019) 19254-19261.
- [20] V. Romano, A. Agresti, R. Verduci, G. D'Angelo, Advances in perovskites for photovoltaic applications in space, *ACS Energy Letters* 7(8) (2022) 2490-2514.
- [21] L. Pan, G. Zhu, Perovskite materials: synthesis, characterisation, properties, and applications, *BoD-Books on Demand* 2016.
- [22] N. Liedienov, I. Fesyeh, A. Pashchenko, D. Tatarchuk, V. Kladko, Magnetotransport and dielectric properties of Bi-containing $\text{La}_{0.6}\text{Sr}_{0.15}\text{Bi}_{0.15}\text{Mn}_{1.1-x}\text{B}_x\text{O}_{3-\delta}$ rare-earth manganites with $B = \text{Cr, Fe, Co, Ni}$, 2017 IEEE International Young Scientists Forum on Applied Physics and Engineering (YSF), IEEE, 2017, pp. 179-182.
- [23] A. Pashchenko, N. Liedienov, I. Fesyeh, Q. Li, V. Pitsyuga, V. Turchenko, V. Pogrebnyak, B. Liu, G. Levchenko, Smart magnetic nanopowder based on the manganite perovskite for local hyperthermia, *RSC advances* 10(51) (2020) 30907-30916.
- [24] F. Saadaoui, R. M'nassri, H. Omrani, M. Koubaa, N.C. Boudjada, A. Cheikhrouhou, Critical behavior and magnetocaloric study in $\text{La}_{0.6}\text{Sr}_{0.4}\text{CoO}_3$ cobaltite prepared by a sol-gel process, *RSC Advances* 6(56) (2016) 50968-50977.
- [25] C. Rao, O. Parkash, D. Bahadur, P. Ganguly, S. Nagabhushana, Itinerant electron ferromagnetism in Sr^{2+} -, Ca^{2+} -, and Ba^{2+} -doped rare-earth orthocobaltites ($\text{Ln}^{3+}_{1-x}\text{M}^{2+}_x\text{CoO}_3$), *Journal of Solid State Chemistry* 22(3) (1977) 353-360.

- [26] D. Bhoi, N. Khan, A. Midya, M. Nandi, A. Hassen, P. Choudhury, P. Mandal, Formation of nanosize griffiths-like clusters in solid solution of ferromagnetic manganite and cobaltite, *The Journal of Physical Chemistry C* 117(32) (2013) 16658-16664.
- [27] Y. Zhu, W. Zhou, Z.G. Chen, Y. Chen, C. Su, M.O. Tadé, Z. Shao, SrNb_{0.1}Co_{0.7}Fe_{0.2}O_{3-δ} perovskite as a next-generation electrocatalyst for oxygen evolution in alkaline solution, *Angewandte Chemie* 127(13) (2015) 3969-3973.
- [28] R. Xie, Z. Nie, X. Hu, Y. Yu, C. Aruta, N. Yang, P.-d. LaCoO, toward stable and efficient oxygen evolution reaction. *ACS Appl, Energy Mater* 4(9) (2021) 9057-9065.
- [29] A. Vignesh, M. Prabu, S. Shanmugam, Porous LaCo_{1-x}Ni_xO_{3-δ} nanostructures as an efficient electrocatalyst for water oxidation and for a zinc–air battery, *ACS applied materials & interfaces* 8(9) (2016) 6019-6031.
- [30] T.X. Nguyen, Y.C. Liao, C.C. Lin, Y.H. Su, J.M. Ting, Advanced high entropy perovskite oxide electrocatalyst for oxygen evolution reaction, *Advanced Functional Materials* 31(27) (2021) 2101632.
- [31] Y. Lu, A. Ma, Y. Yu, R. Tan, C. Liu, P. Zhang, D. Liu, J. Gui, Engineering oxygen vacancies into LaCoO₃ perovskite for efficient electrocatalytic oxygen evolution, *ACS Sustainable Chemistry & Engineering* 7(3) (2018) 2906-2910.
- [32] Y. Liang, Y. Cui, Y. Chao, N. Han, J. Sunarso, P. Liang, X. He, C. Zhang, S. Liu, Exsolution of CoFe (Ru) nanoparticles in Ru-doped (La_{0.8}Sr_{0.2})_{0.9}Co_{0.1}Fe_{0.8}Ru_{0.1}O_{3-δ} for efficient oxygen evolution reaction, *Nano Research* 15(8) (2022) 6977-6986.
- [33] L. Yu, N. Xu, T. Zhu, Z. Xu, M. Sun, D. Geng, La_{0.4}Sr_{0.6}Co_{0.7}Fe_{0.2}Nb_{0.1}O_{3-δ} perovskite prepared by the sol-gel method with superior performance as a bifunctional oxygen electrocatalyst, *International Journal of Hydrogen Energy* 45(55) (2020) 30583-30591.
- [34] D. Ji, C. Liu, Y. Yao, L. Luo, W. Wang, Z. Chen, Cerium substitution in LaCoO₃ perovskite oxide as bifunctional electrocatalysts for hydrogen and oxygen evolution reactions, *Nanoscale* 13(22) (2021) 9952-9959.
- [35] W. Guo, L. Cui, H. Xu, C. Gong, Selective dissolution of A-site cations of La_{0.6}Sr_{0.4}Co_{0.8}Fe_{0.2}O₃ perovskite catalysts to enhance the oxygen evolution reaction, *Applied Surface Science* 529 (2020) 147165.
- [36] X. Jiang, Y. Dong, Z. Zhang, J. Li, J. Qian, D. Gao, Cation substitution of B-site in LaCoO₃ for bifunctional oxygen electrocatalytic activities, *Journal of Alloys and Compounds* 878 (2021) 160433.
- [37] R. Majee, S. Chakraborty, H.G. Salunke, S. Bhattacharyya, Maneuvering the physical properties and spin states to enhance the activity of La–Sr–Co–Fe–O perovskite oxide nanoparticles in electrochemical water oxidation, *ACS Applied Energy Materials* 1(7) (2018) 3342-3350.
- [38] M. Álvarez-Galván, V. de La Peña O'Shea, G. Arzamendi, B. Pawelec, L. Gandía, J. Fierro, Methyl ethyl ketone combustion over La-transition metal (Cr, Co, Ni, Mn) perovskites, *Applied Catalysis B: Environmental* 92(3-4) (2009) 445-453.
- [39] S. Zhou, X. Miao, X. Zhao, C. Ma, Y. Qiu, Z. Hu, J. Zhao, L. Shi, J. Zeng, Engineering electrocatalytic activity in nanosized perovskite cobaltite through surface spin-state transition, *Nature communications* 7(1) (2016) 11510.
- [40] C.-F. Chen, G. King, R.M. Dickerson, P.A. Papin, S. Gupta, W.R. Kellogg, G. Wu, Oxygen-deficient BaTiO_{3-x} perovskite as an efficient bifunctional oxygen electrocatalyst, *Nano Energy* 13 (2015) 423-432.
- [41] X. Gu, H. Jing, X. Mu, H. Yang, Q. Zhou, S. Yan, S. Liu, C. Chen, La-triggered synthesis of oxygen vacancy-modified cobalt oxide nanosheets for highly efficient oxygen evolution in alkaline media, *Journal of Alloys and Compounds* 814 (2020) 152274.
- [42] W. Shen, J. Jin, Y. Hu, Y. Hou, J. Yin, Z. Ma, Y.-Q. Zhao, P. Xi, Surface chlorine doped perovskite-type cobaltate lanthanum for water oxidation, *Chinese Journal of Catalysis* 43(6) (2022) 1485-1492.
- [43] W. Li, Y. Zhu, W. Guo, H. Xu, C. Gong, G. Xue, Enhanced oxygen and hydrogen evolution activities of Pt/LaCoO₃ perovskite oxide via in-situ exsolution of Pt nanoparticles, *Journal of Chemical Sciences* 134(2) (2022) 38.

- [44] Z. Li, Y. Xie, Z. Huang, Y. Su, C. Sun, J. Fu, H. Wei, F. Wu, G. Ou, Amorphization of LaCoO₃ Perovskite Nanostructures for Efficient Oxygen Evolution, *ACS Applied Nano Materials* 5(10) (2022) 14209-14215.
- [45] Z. Wei, A. Pashchenko, N. Liedienov, I. Zatovsky, D. Butenko, Q. Li, I. Fesych, V. Turchenko, E. Zubov, P.Y. Polynchuk, Multifunctionality of lanthanum–strontium manganite nanopowder, *Physical Chemistry Chemical Physics* 22(21) (2020) 11817-11828.
- [46] Z. Gong, W. Xu, N. Liedienov, D. Butenko, I. Zatovsky, I. Gural'skiy, Z. Wei, Q. Li, B. Liu, Y.A. Batman, Expansion of the multifunctionality in off-stoichiometric manganites using post-annealing and high pressure: Physical and electrochemical studies, *Physical Chemistry Chemical Physics* 24(36) (2022) 21872-21885.
- [47] I.V. Odynets, N.Y. Strutynska, J. Li, W. Han, I.V. Zatovsky, N. Klyui, CoO_x(OH)_y/C nanocomposites in situ derived from Na₄Co₃(PO₄)₂P₂O₇ as sustainable electrocatalysts for water splitting, *Dalton Transactions* 47(44) (2018) 15703-15713.
- [48] H. Rietveld, Line profiles of neutron powder-diffraction peaks for structure refinement, *Acta Crystallographica* 22(1) (1967) 151-152.
- [49] C. Frontera, J. Rodríguez-Carvajal, FullProf as a new tool for flipping ratio analysis, *Physica B: Condensed Matter* 335(1-4) (2003) 219-222.
- [50] Z. Wei, N. Liedienov, Q. Li, A. Pashchenko, W. Xu, V. Turchenko, M. Yuan, I. Fesych, G. Levchenko, Influence of post-annealing, defect chemistry and high pressure on the magnetocaloric effect of non-stoichiometric La_{0.8-x}K_{0.2}Mn_{1+x}O₃ compounds, *Ceramics International* 47(17) (2021) 24553-24563.
- [51] M. Yuan, G. Levchenko, Q. Li, L. Berezhnaya, H. Fylymonov, A.B. Gaspar, M. Seredyuk, J.A. Real, Variable cooperative interactions in the pressure and thermally induced multistep spin transition in a two-dimensional iron (II) coordination polymer, *Inorganic Chemistry* 59(15) (2020) 10548-10556.
- [52] T. Takeda, H. Watanabe, Magnetic properties of the system SrCo_{1-x}Fe_xO_{3-y}, *Journal of the Physical Society of Japan* 33(4) (1972) 973-978.
- [53] H. Taguchi, M. Shimada, M. Koizumi, The effect of oxygen vacancy on the magnetic properties in the system SrCoO_{3-δ} (0 < δ < 0.5), *Journal of Solid State Chemistry* 29(2) (1979) 221-225.
- [54] J. Lim, J. Yu, Role of oxygen vacancy in the spin-state change and magnetic ordering in SrCoO_{3-δ}, *Physical Review B* 98(8) (2018) 085106.
- [55] S. Chowdhury, R.J. Choudhary, D.M. Phase, Spectroscopic aspects of the magnetic interaction in SrCoO_{2.75} and SrCoO₃ thin films, *Journal of Alloys and Compounds* 869 (2021) 159296.
- [56] L. Hao, Z. Zhang, X. Xie, H. Wang, Q. Yu, H. Zhu, Preparation of SrCoO_x thin films on LaAlO₃ substrate and their reversible redox process at moderate temperatures, *Journal of Crystal Growth* 427 (2015) 36-41.
- [57] Q. Xie, Z. Wu, X. Wu, W. Tan, Sr content on the structure and magnetic properties of La_{1-x}Sr_xCoO₃, *Journal of alloys and compounds* 474(1-2) (2009) 81-85.
- [58] <http://abulafia.mt.ic.ac.uk/shannon/ptable.php>
- [59] J.I. Langford, A. Wilson, Scherrer after sixty years: a survey and some new results in the determination of crystallite size, *Journal of applied crystallography* 11(2) (1978) 102-113.
- [60] J.B. Goodenough, Coexistence of localized and itinerant d electrons, *Materials Research Bulletin* 6(10) (1971) 967-976.
- [61] N.A. Liedienov, Z. Wei, V.M. Kalita, A.V. Pashchenko, Q. Li, I.V. Fesych, V.A. Turchenko, C. Hou, X. Wei, B. Liu, Spin-dependent magnetism and superparamagnetic contribution to the magnetocaloric effect of non-stoichiometric manganite nanoparticles, *Applied Materials Today* 26 (2022) 101340.
- [62] A. Pashchenko, V. Pashchenko, V. Prokopenko, V. Turchenko, Y.F. Revenko, A. Mazur, V.Y. Sycheva, N. Liedienov, V. Pitsyuga, G. Levchenko, Role of structure imperfection in the formation of the magnetotransport properties of rare-earth manganites with a perovskite structure, *Journal of Experimental and Theoretical Physics* 124 (2017) 100-113.

- [63] F. Tournus, E. Bonet, Magnetic susceptibility curves of a nanoparticle assembly, I: Theoretical model and analytical expressions for a single magnetic anisotropy energy, *Journal of Magnetism and Magnetic Materials* 323(9) (2011) 1109-1117.
- [64] F. Tournus, A. Tamion, Magnetic susceptibility curves of a nanoparticle assembly II. Simulation and analysis of ZFC/FC curves in the case of a magnetic anisotropy energy distribution, *Journal of Magnetism and Magnetic Materials* 323(9) (2011) 1118-1127.
- [65] N. Liedienov, V. Kalita, A. Pashchenko, Y.I. Dzhezherya, I. Fesych, Q. Li, G. Levchenko, Critical phenomena of magnetization, magnetocaloric effect, and superparamagnetism in nanoparticles of non-stoichiometric manganite, *Journal of Alloys and Compounds* 836 (2020) 155440.
- [66] A. Ignatenko, V.Y. Irkhin, Size and surface effects on the magnetism of magnetite and maghemite nanoparticles, *Journal of Experimental and Theoretical Physics* 124(2) (2017).
- [67] N. Zhang, W. Ding, W. Zhong, D. Xing, Y. Du, Tunnel-type giant magnetoresistance in the granular perovskite $\text{La}_{0.85}\text{Sr}_{0.15}\text{MnO}_3$, *Physical Review, B: Condensed Matter* 56(13) (1997).
- [68] F. Liu, Y. Gao, H. Chang, Y. Liu, Y. Yun, Control of magnetic properties and band gap by Co/Mn ordering and oxygen distributions of $\text{La}_2\text{CoMnO}_6$, *Journal of Magnetism and Magnetic Materials* 435 (2017) 217-222.
- [69] B. Banerjee, On a generalised approach to first and second order magnetic transitions, *Physics letters* 12(1) (1964) 16-17.
- [70] A.M. Tishin, Y.I. Spichkin, *The magnetocaloric effect and its applications*, CRC Press 2016.
- [71] D.S. Butenko, S. Li, R. Chen, I.V. Odynets, D. Li, Z. Yuan, X. Zhang, I. Zatonvsky, $\text{Na}_4\text{Co}_3\text{P}_4\text{O}_{15}$ in situ transformation to $\text{Co}(\text{OH})_2/\text{CoO}(\text{OH})$ nanoforms for aqueous supercapacitor using redox additive electrolyte, *Materials Science and Engineering: B* 286 (2022) 116051.
- [72] C. Mu, D.S. Butenko, I.V. Odynets, I.V. Zatonvsky, J. Li, W. Han, N.I. Klyui, $\text{Na}_4\text{Ni}_3\text{P}_4\text{O}_{15}$ - $\text{Ni}(\text{OH})_2$ core-shell nanoparticles as hybrid electrocatalysts for the oxygen evolution reaction in alkaline electrolytes, *Dalton Transactions* 49(24) (2020) 8226-8237.
- [73] Y.Z. Vassilyeva, D.S. Butenko, S. Li, W. Han, A.Y. Pak, Synthesis of molybdenum carbide catalyst by DC arc plasma in ambient air for hydrogen evolution, *Materials Chemistry and Physics* 254 (2020) 123509.
- [74] F. Fang, P. Zhao, N. Feng, H. Wan, G. Guan, Surface engineering on porous perovskite-type $\text{La}_{0.6}\text{Sr}_{0.4}\text{CoO}_{3-\delta}$ nanotubes for an enhanced performance in diesel soot elimination, *Journal of Hazardous Materials* 399 (2020) 123014.
- [75] R. Zeng, Y. Huang, Enhancing surface activity of $\text{La}_{0.6}\text{Sr}_{0.4}\text{CoO}_{3-\delta}$ cathode by a simple infiltration process, *International Journal of Hydrogen Energy* 42(10) (2017) 7220-7225.
- [76] C. Vaz, D. Prabhakaran, E. Altman, V. Henrich, Experimental study of the interfacial cobalt oxide in $\text{Co}_3\text{O}_{4/\alpha}$ - Al_2O_3 (0001) epitaxial films, *Physical Review B* 80(15) (2009) 155457.
- [77] J.-C. Dupin, D. Gonbeau, P. Vinatier, A. Levasseur, Systematic XPS studies of metal oxides, hydroxides and peroxides, *Physical Chemistry Chemical Physics* 2(6) (2000) 1319-1324.
- [78] H. Wang, X. Chen, D. Huang, M. Zhou, D. Ding, H. Luo, Cation deficiency tuning of LaCoO_3 perovskite as bifunctional oxygen electrocatalyst, *ChemCatChem* 12(10) (2020) 2768-2775.
- [79] F. Zhou, Z. Zhao, M. Xu, T. Wang, H. Yang, R. Wang, J. Wang, H. Li, M. Feng, The Spin Modulation Stimulated Efficient Electrocatalytic Oxygen Evolution Reaction over LaCoO_3 Perovskite, *Chemistry—A European Journal* 28(14) (2022) e202104157.

Electronic Supplementary Information

The multifunctionality of lanthanum-strontium cobaltite nanopowder: high-pressure magnetic and excellent electrocatalytic properties for OER

Hanlin Yu^a, N.A. Liedienov^{a,b,*}, I.V. Zatonovsky^c, D.S. Butenko^{d,e,*}, I.V. Fesych^f, Wei Xu^g,
Songchun Rui^h, Quanjun Li^a, Bingbing Liu^a, A.V. Pashchenko^{a,c,i}, G.G. Levchenko^{a,c,*}

^aState Key Laboratory of Superhard Materials, International Center of Future Science, Jilin University, 130012 Changchun, P.R. China

^bDonetsk Institute for Physics and Engineering named after O.O. Galkin, NASU, 03028 Kyiv, Ukraine

^cF.D. Ovcharenko Institute of Biocolloidal Chemistry, NASU, 03142 Kyiv, Ukraine

^dShenzhen Key Laboratory of Solid State Batteries, Southern University of Science and Technology, Shenzhen 518055, P.R. China

^eAcademy for Advanced Interdisciplinary Studies, Southern University of Science and Technology, Shenzhen 518055, P.R. China

^fTaras Shevchenko National University of Kyiv, 01030 Kyiv, Ukraine

^gState Key Laboratory of Inorganic Synthesis and Preparative Chemistry, College of Chemistry, Jilin University, Changchun, 130012, P.R. China

^hBaicheng Normal University, 137099 Baicheng, China

ⁱInstitute of Magnetism NASU and MESU, 03142 Kyiv, Ukraine

*Corresponding author

E-mail address: nikita.ledenev.ssp@gmail.com (N.A. Liedienov)

debut98@ukr.net (D.S. Butenko)

g-levch@ukr.net (G.G. Levchenko)

Determination of the size of the coherent scattering region in the $\text{La}_{0.6}\text{Sr}_{0.4}\text{CoO}_3$ nanopowders

The size of the coherent scattering region D_{XRD} was determined using the X-ray line broadening method. The average size D_{XRD} in the $\text{La}_{0.6}\text{Sr}_{0.4}\text{CoO}_3$ (LSCO) nanopowders is related to the dimensional broadening of β for diffraction reflection (012) according to the Scherrer equation [1]:

$$D_{\text{XRD}} = K\lambda / \beta \cos\theta, \quad (\text{S1})$$

where D_{XRD} is the size of scattering crystallites in nm; $\lambda = 0.15406$ nm is the wavelength of X-ray radiation; $K = 0.9$ is a constant that depends on the method for determining the line broadening and crystal shape; β is the width of the intensity distribution curve at half of the height of the maximum of the reflex in radians; θ is the diffraction angle in degrees.

Considering that the integral width of the peak in the diffractogram is approximated by the pseudo-Voigt function with a large (up to 90% or more) contribution of the Lorentz function, the Lorentzian was used to describe the shape of the diffraction reflection at $2\theta \approx 23.2^\circ$ (see Fig.S1). In order to exclude the instrumental broadening β_{inst} , standard silicon (Si) X-ray powder diffraction data (JCPDS89-2955) was recorded under the same condition in a separate experiment. The integral width of the peak was calculated by the formula [2]:

$$\beta_{012} = \beta_{\text{exp}} - \beta_{\text{inst}}, \quad (\text{S2})$$

where β_{exp} is the experimental width of the sample peak at half the maximum intensity; β_{inst} is an instrumental broadening of the diffraction line, which depends on the design features of the diffractometer (in radians).

The average size of the D_{XRD} was obtained using an approximation of the experimental values of the intensity of the diffraction maximum with a Bragg angle of $2\theta \approx 23.2^\circ$ and considering all the experimental parameters in equation (S1) (see Table S1).

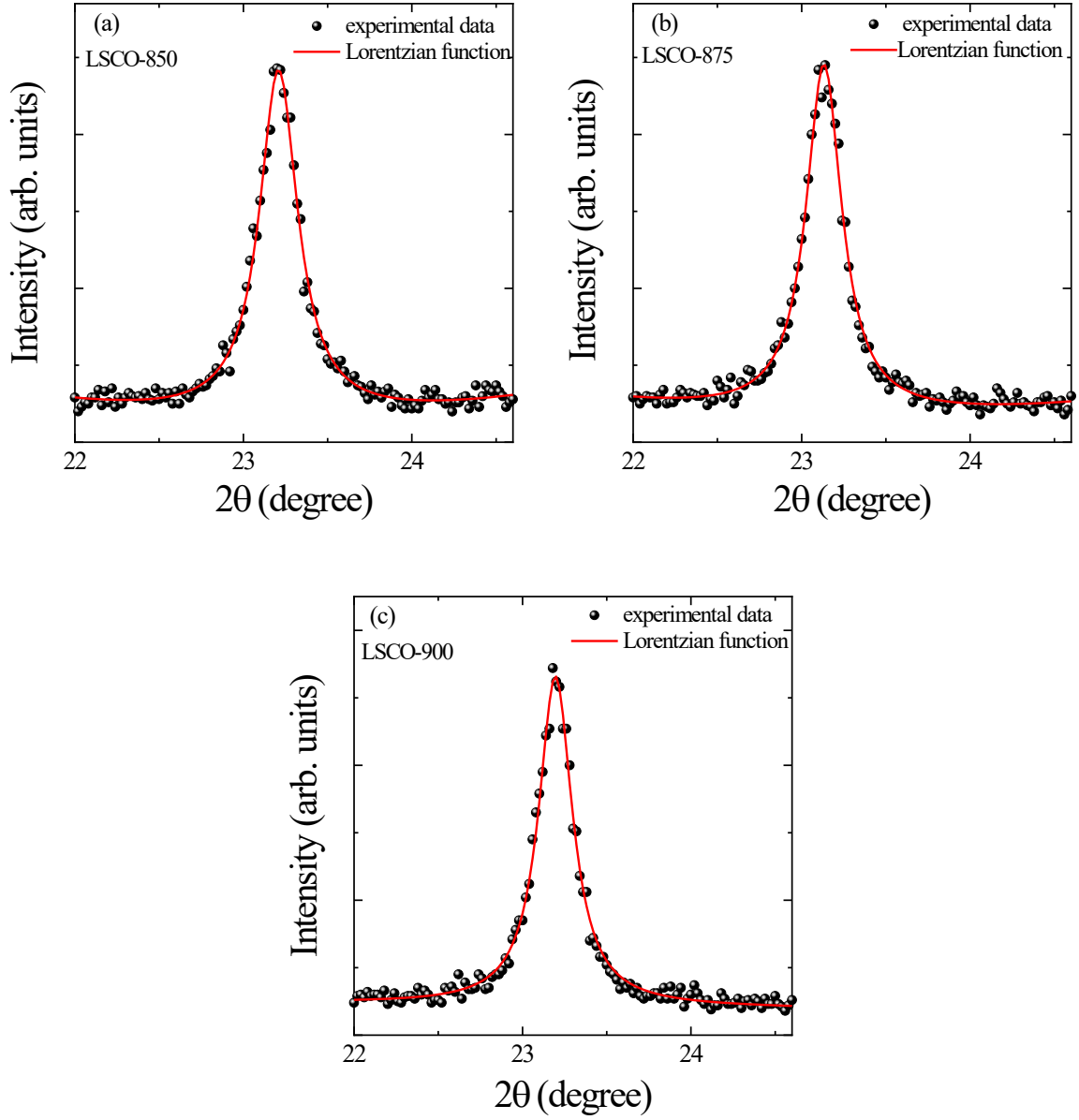


Fig. S1. The diffraction patterns and their approximation by Lorentzian function for the LSCO nanpowders in the region of the (012) reflection with an angle of $2\theta \approx 23.2^\circ$.

Table S1

The experimental parameters in Eq. (S1) and the average size of the coherent scattering regions D_{XRD} for the LSCO nanpowders with different annealing temperatures t_{ann} .

t_{ann} ($^\circ\text{C}$)	2θ (degree)	β (radian)	$\cos\theta$	λ (nm)	K	D_{XRD} (nm)
850	23.208	0.0030	0.97956	0.15406	0.9	48 ± 1
875	23.132	0.0026	0.97969	0.15406	0.9	54 ± 1
900	23.195	0.0024	0.97958	0.15406	0.9	60 ± 1

Electrochemical properties of the LSCO nanopowders

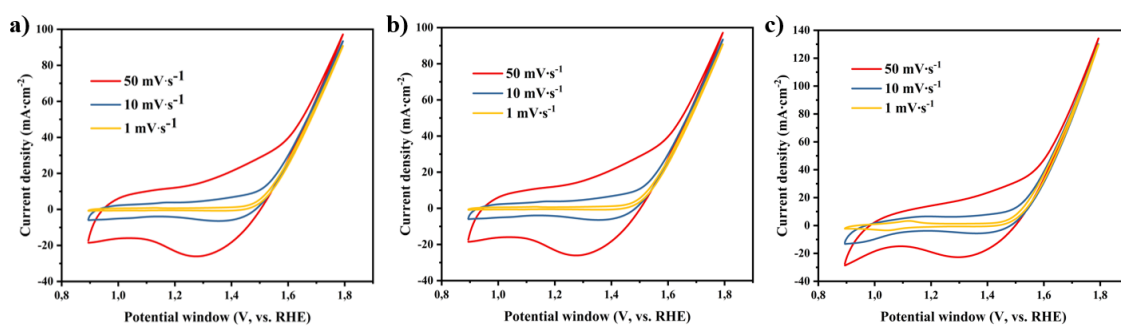


Fig. S2. CV curves at different scanning rates for LSCO electrodes: (a) LSCO-850, (b) LSCO-875, (c) LSCO-900.

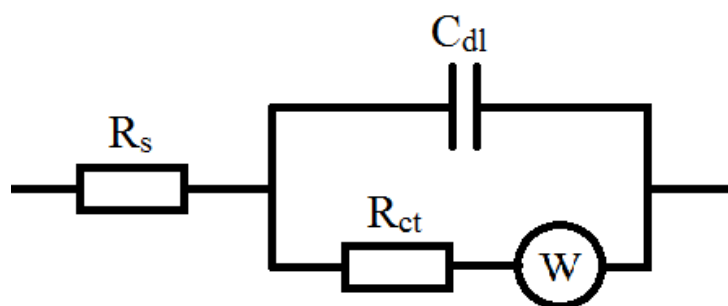


Fig. S3. The equivalent scheme for EIS measurement.

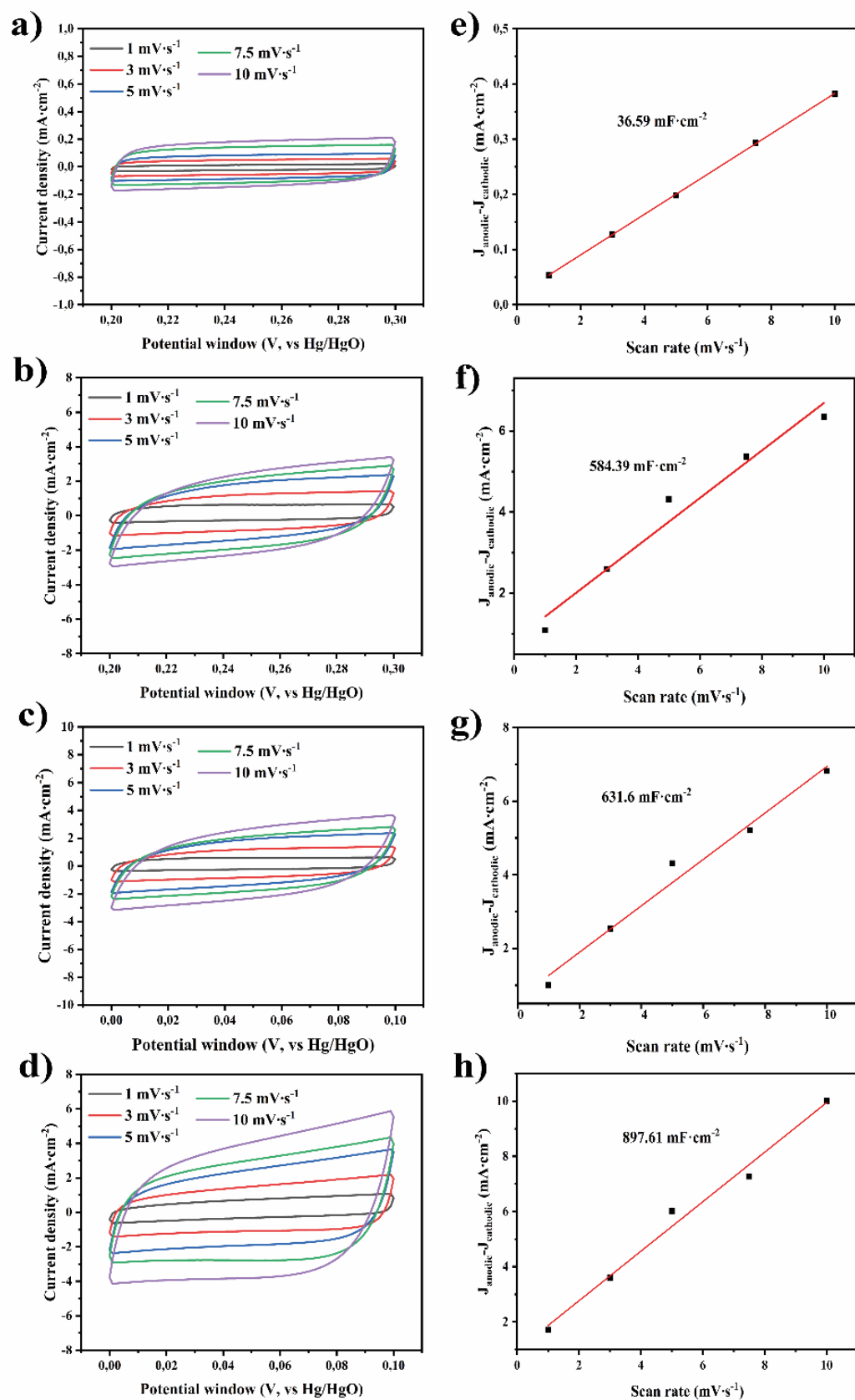


Fig. S4. Cyclic voltammograms of (a) LSCO-850, (b) LSCO-875, (c) LSCO-900, and (d) carbon fiber at different scan rates in the voltage range of 0–0.1 V. Δj versus RHE as a function of the scan rate for the (e) LSCO-850, (f) LSCO-875, (g) LSCO-900, and (h) carbon fiber.

The double-layer capacitance C_{dl} was estimated by plotting the Δj versus RHE as a function of the scan rate (Fig. S4 (e-h)): $C_{dl} = d(\Delta j)/(2dV)$. The ECSA can be calculated from the C_{dl} according to $ECSA = C_{dl}/C_s$ (C_s is the specific capacitance of a flat surface with 1 cm² of real surface area). In this case, CC-based with Super P electrode can be accepted as a standard, showing the measured capacitance of 36.59 mF·cm⁻². The ECSA values of LSCO-850, LSCO-875, and LSCO-900 are 15.97 cm², 17.26 cm², and 24.53 cm², respectively.

Table S2

Overpotential OER and Tafel slope values for LSCO samples according to LSV tests.

Sample	Overpotential OER			Tafel slope (mV·dec ⁻¹)
	η_{10} (mV)	η_{20} (mV)	η_{100} (mV)	
	<i>Initial values</i>			
LSCO-850	285	310	379	74.7
LSCO-875	275	296	360	80.9
LSCO-900	265	290	360	81.7
RuO ₂	320	356	534	92.6
	<i>After 24 h of incessant electrolysis (current density 10 mA·cm⁻²)</i>			
LSCO-850	362	401	543	121.8
LSCO-875	335	363	444	94.7
LSCO-900	312	338	410	87.7
	<i>Change in LSV value after CP test (current density 10 mA·cm⁻²), %</i>			
LSCO-850	+27.0	+29.4	+43.3	–
LSCO-875	+21.8	+22.6	+23.3	–
LSCO-900	+17.7	+16.6	+13.9	–

Table S3

The value of overpotential OER during electrolysis for LSCO samples according to the results of the CP tests.

Sample	Electrolysis time (h)				
	0	1	4	12	24
LSCO-850	285	317 (+32)	335 (+50)	346 (+61)	362 (+77)
LSCO-875	275	307 (+32)	320 (+45)	328 (+53)	334 (+64)
LSCO-900	265	288 (+23)	300 (+35)	306 (+41)	312 (+47)

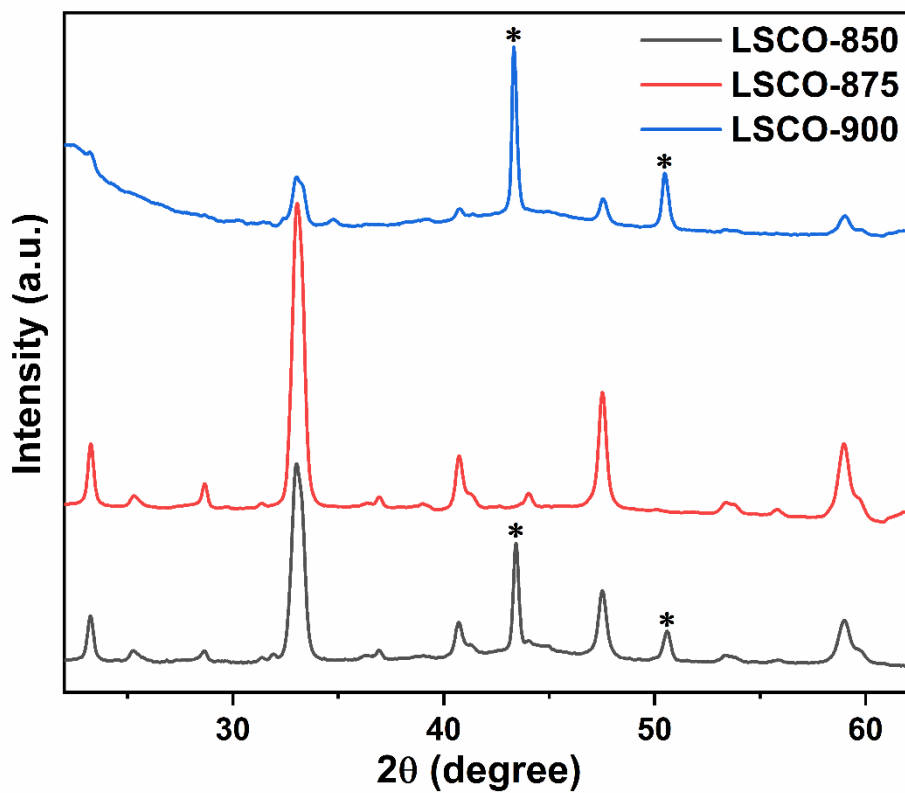


Fig. S5. The XRD results for the LSCO electrode after the CP test in 1 M KOH electrolyte (* diffraction reflexes of metallic copper caused by the copper holder of the electrode material).

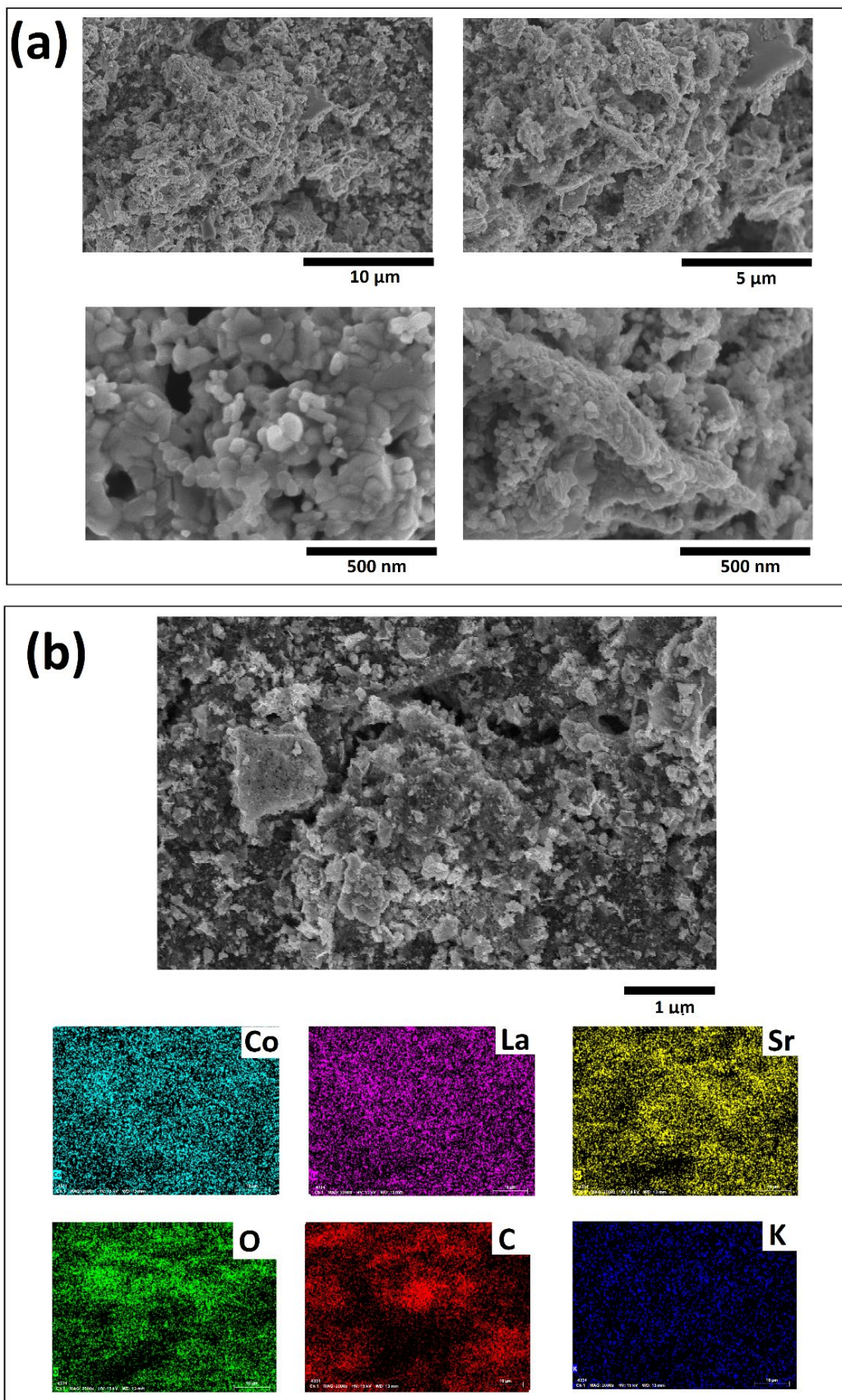


Fig. S6. SEM images and mapping of surface elements of the LSCO-850 electrode after long-term electrolysis.

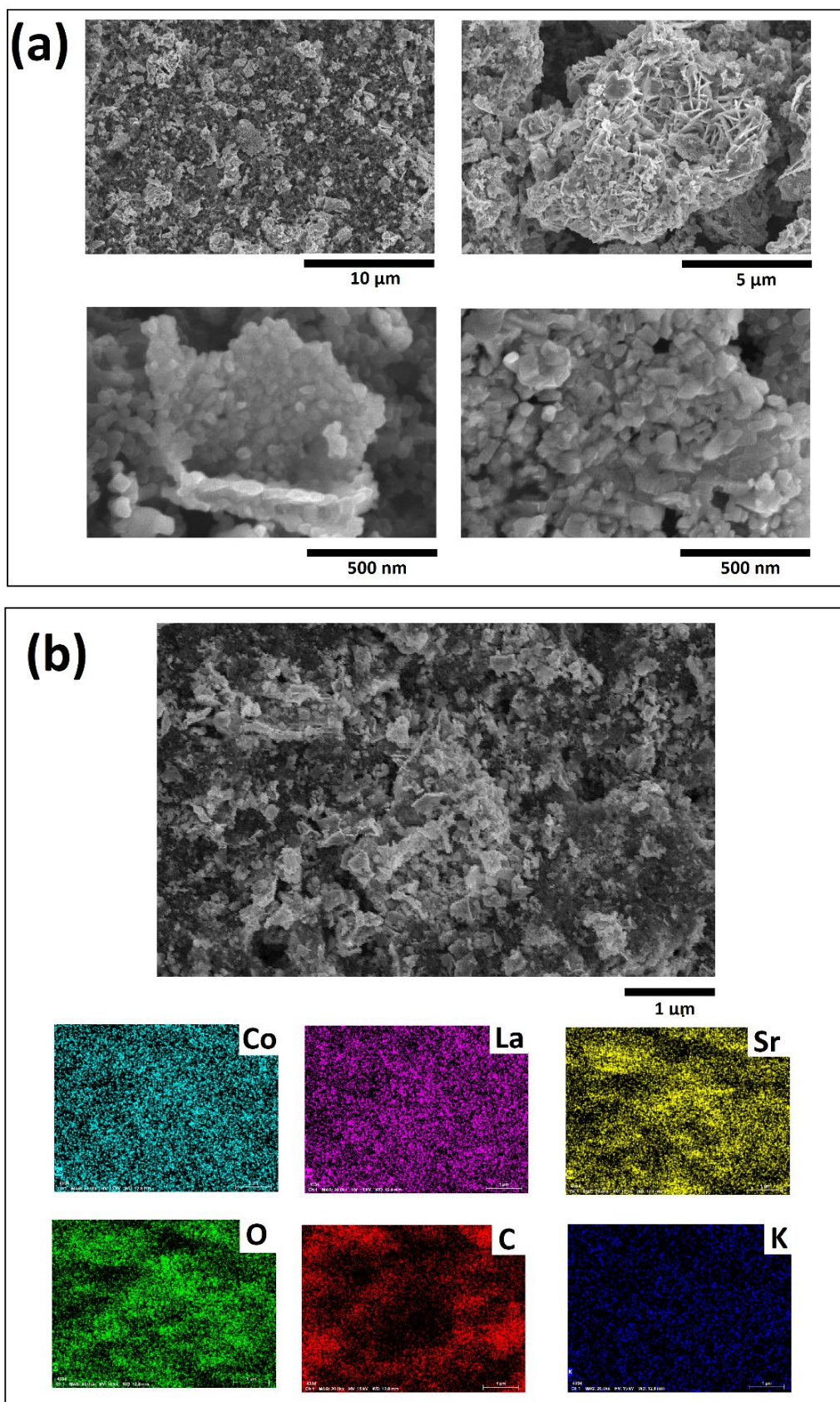


Fig. S7. SEM images and mapping of surface elements of the LSCO-875 electrode after long-term electrolysis.

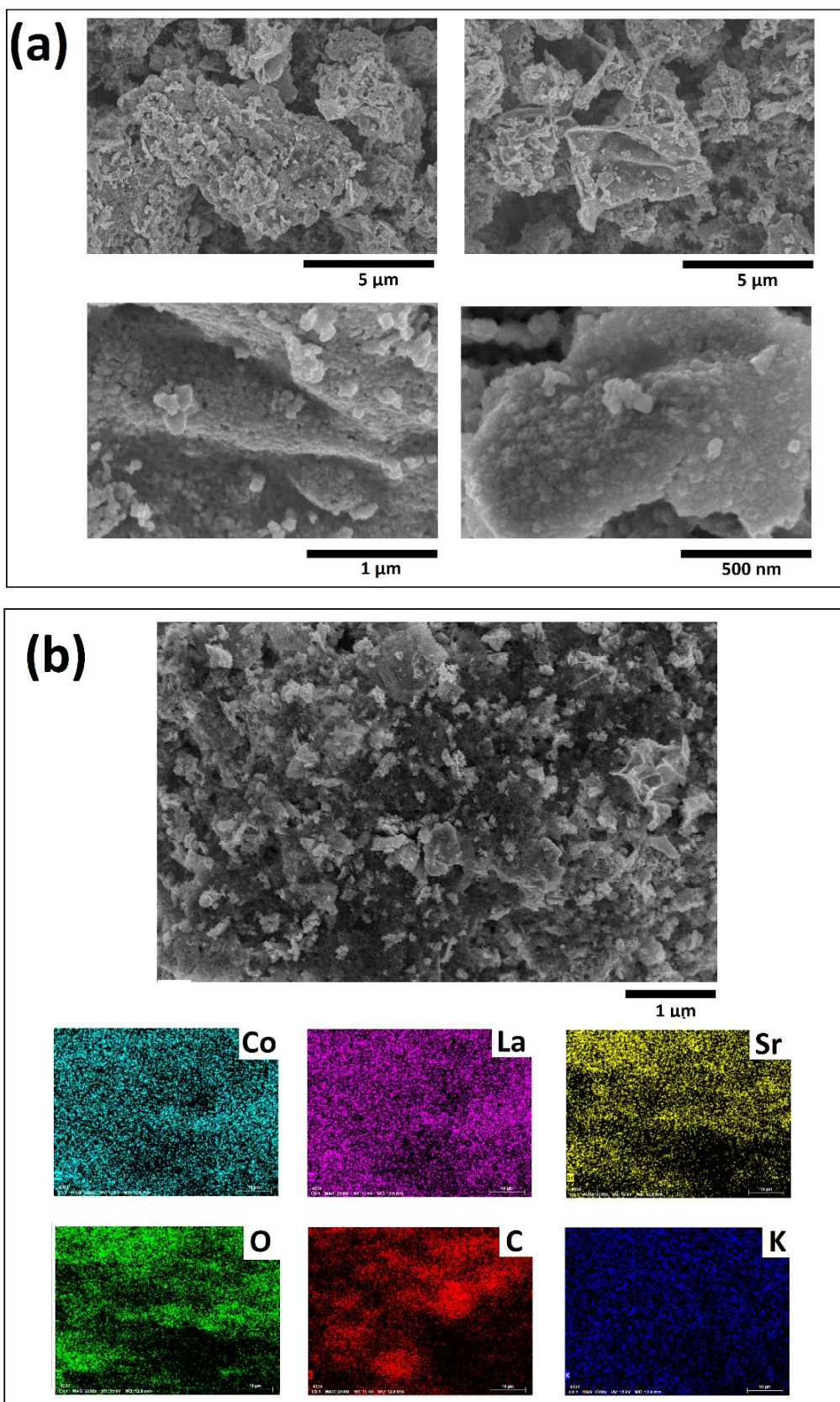


Fig. S8. SEM images and mapping of surface elements of the LSCO-900 electrode after long-term electrolysis.

XPS of the LSCO-900 nanopowders

The survey spectra of the LSCO-900 samples before and after electrocatalysis show the existence of La, Sr, Co, and O peaks (Fig. S9(a)). At first glance, they seem very similar, but as shown below, an amorphous state of the LSCO-900 after electrocatalysis has been detected. In the high-resolution XPS spectra of the La3d, two major peaks, corresponding spin doublet La3d_{5/2} and La3d_{3/2}, are observed (Fig. S9(b)). However, the spectra have a more complex profile due to charge transfer satellites, plasmon lines, and MNN Auger lines (marked as A and B in Fig. S9(b)). Similar results are also observed for the XPS spectrum of La₂O₃ [3] and La-containing manganite compounds [4]. The binding energy positions for the LSCO-900 before electrocatalysis are 832.9 eV (La3d_{5/2}) and 849.8 eV (La3d_{3/2}), with a difference of 16.8 eV which agrees with the standard deviation [5]. All La ions are in a trivalent state. Noteworthy, the XPS spectrum for the LSCO-900 after electrocatalysis is transformed to single-peaks with the binding energies of 833.3 (La3d_{5/2}) and 850.9 eV (La3d_{3/2}). It is associated with the amorphization of the LSCO-900 surface and the appearance of chemical defects due to a positive core-level shift of 0.4–0.9 eV [6]. All peak positions for the La, Sr, and O ions are listed in Table S4.

Fig. S9(c) shows Sr3d spectra decomposed to two main components from the perovskite lattice-bound Sr_{lat} at lower binding energies (131.6 for 3d_{5/2} and 133.4 eV for 3d_{3/2}) and from the surface-bound Sr_{surf} at higher binding energies (133.5 for 3d_{5/2} and 135.3 eV for 3d_{3/2}) for the LSCO-900 before electrocatalysis (see Table S4). The peak positions agree with other literature data [7, 8]. The surfaced Sr_{surf} may be attributed to the formation of SrCO₃, SrO, and Sr(OH)₂ [9-11]. As it turned out, the Sr_{surf} / Sr_{lat} before and after electrochemical tests are 1.4 and 3, respectively. Moreover, a positive core-level shift of 1.9 eV is observed, showing the presence of oxygen vacancies. Additionally, after electrocatalysis, the three main peaks of Sr are transformed to somehow one single-peak. All this indicates an amorphization of the LSCO-900 surface as well.

As for O1s XPS before and after electrochemical tests (Fig. S9(d)), three components with energy positions of about 528.1–528.4 (O1), 530.0–531.2 (O2), and 531.2–533.8 (O3) eV can be distinguished in the spectra (see Table S4). Peak O1 should be attributed to the lattice oxygen, while components O2 and O3 are due to adsorbed oxygen and hydroxyl groups or water on the surface, respectively [6]. It should be noted that the ratio of $O_{\text{ads}} / O_{\text{lat}}$ before and after electrocatalysis increases by 2.3 and 2.5, respectively. Moreover, O3 contribution after electrocatalysis increases significantly, indicating growth in H_2O molecules.

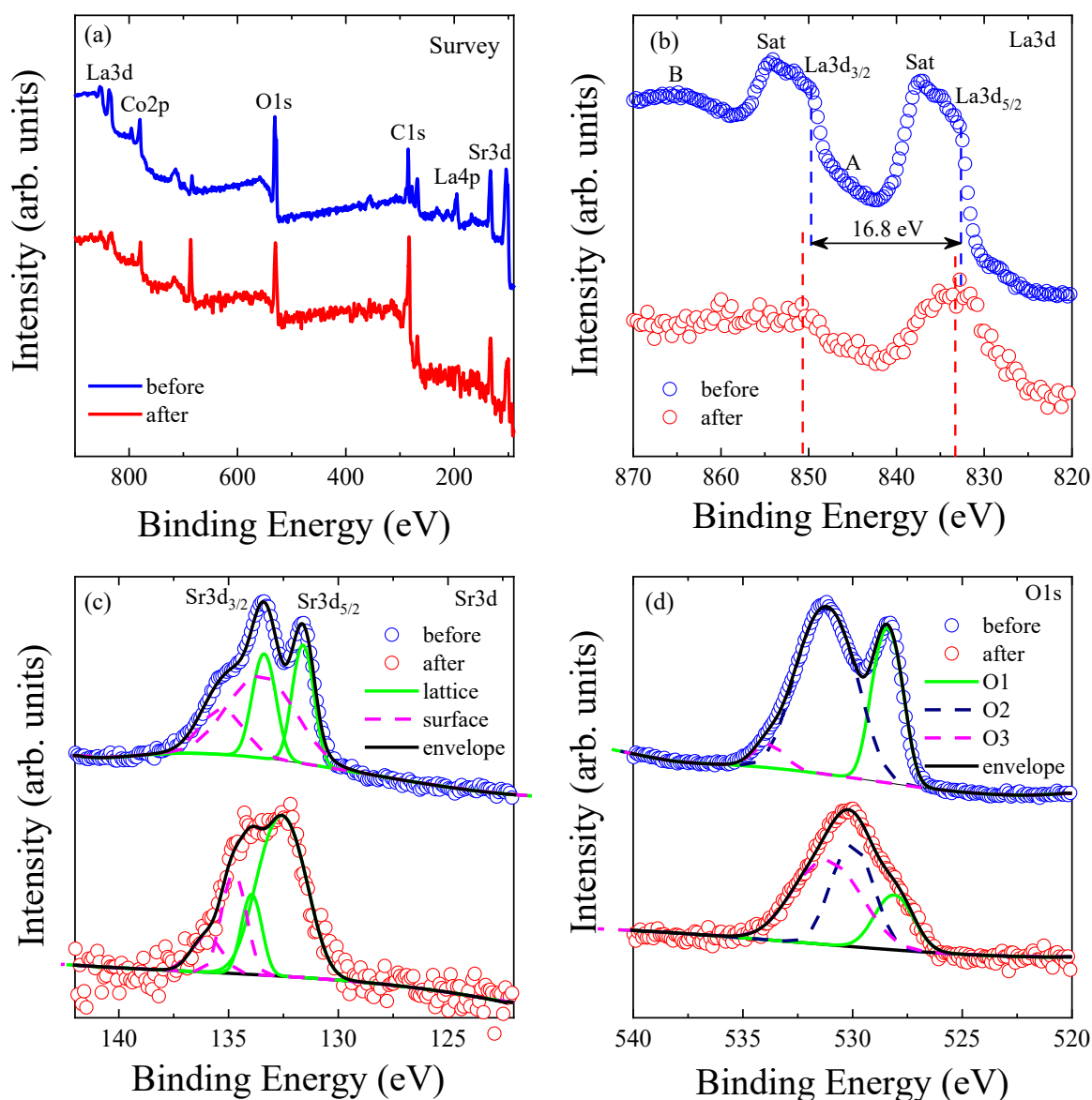


Fig. S9. XPS curves for the LSCO-900 samples before and after electrocatalysis: (a) survey spectra; (b) La3d spectra; (c) Sr3d spectra; and (d) O1s spectra.

Table S4

Energy positions of the La3d, Sr3d, and O1s X-ray photoelectron lines in the LSCO-900 samples before and after electrocatalysis.

Electro-catalysis	Binding energy (eV)										
	La3d				Sr3d				O1s		
	La3d _{5/2}	Sat	La3d _{3/2}	Sat	Sr _{lat} 5/2	Sr _{surf} 5/2	Sr _{lat} 3/2	Sr _{surf} 3/2	O1	O2	O3
Before	832.9	837.4	849.8	854.3	131.6	133.4	133.5	135.3	528.4	531.2	533.8
After	833.3		850.9		132.6	133.9	134.8	136.0	528.1	530.0	531.2

Table S5

Energy positions of the Co2p, Co²⁺, and Co₃O₄ X-ray photoelectron lines in the LSCO-900 samples before and after electrocatalysis.

Electrocatalysis	Binding energy (eV)					
	Co2p _{3/2}		Co2p _{1/2}		Co ²⁺	Co ₃ O ₄
	Co ³⁺	Co ⁴⁺	Co ³⁺	Co ⁴⁺	Sat	Sat
Before	780.0	781.7	795.1	796.9	786	789.9
After	778.9	780.8	793.9	795.5	–	789.2

References

- [1] A. Patterson, The Scherrer formula for X-ray particle size determination, *Physical review* 56(10) (1939) 978.
- [2] Th. de Keijser, E.J. Mittemeijer, H.C.F. Rozendaal, The determination of crystallite-size and lattice-strain parameters in conjunction with the profile-refinement method for the determination of crystal structures, *J. Appl. Cryst* 16 (1983) 309-316.
- [3] M. Sunding, K. Hadidi, S. Diplas, O. Løvvik, T. Norby, A. Gunnæs, XPS characterisation of in situ treated lanthanum oxide and hydroxide using tailored charge referencing and peak fitting procedures, *Journal of Electron Spectroscopy and Related Phenomena* 184(7) (2011) 399-409.
- [4] N.A. Liedienov, Z. Wei, V.M. Kalita, A.V. Pashchenko, Q. Li, I.V. Fesych, V.A. Turchenko, C. Hou, X. Wei, B. Liu, Spin-dependent magnetism and superparamagnetic contribution to the magnetocaloric effect of non-stoichiometric manganite nanoparticles, *Applied Materials Today* 26 (2022) 101340.
- [5] F. Fang, P. Zhao, N. Feng, H. Wan, G. Guan, Surface engineering on porous perovskite-type La_{0.6}Sr_{0.4}CoO_{3-δ} nanotubes for an enhanced performance in diesel soot elimination, *Journal of Hazardous Materials* 399 (2020) 123014.
- [6] Z. Li, Y. Xie, Z. Huang, Y. Su, C. Sun, J. Fu, H. Wei, F. Wu, G. Ou, Amorphization of LaCoO₃ Perovskite Nanostructures for Efficient Oxygen Evolution, *ACS Applied Nano Materials* 5(10) (2022) 14209-14215.
- [7] J. Jin, S. Chen, J. Wang, C. Chen, T. Peng, SrCO₃-modified brookite/anatase TiO₂ heterophase junctions with enhanced activity and selectivity of CO₂ photoreduction to CH₄, *Applied Surface Science* 476 (2019) 937-947.
- [8] J.-C. Dupin, D. Gonbeau, P. Vinatier, A. Levasseur, Systematic XPS studies of metal oxides, hydroxides and peroxides, *Physical Chemistry Chemical Physics* 2(6) (2000) 1319-1324.
- [9] P. Van Der Heide, Systematic x-ray photoelectron spectroscopic study of La_{1-x}Sr_x-based perovskite-type oxides, *Surface and Interface Analysis: An International Journal devoted to the development and application of techniques for the analysis of surfaces, interfaces and thin films* 33(5) (2002) 414-425.
- [10] L.T. Hudson, R. Kurtz, S. Robey, D. Temple, R. Stockbauer, Surface core-level shifts of barium observed in photoemission of vacuum-fractured BaTiO₃ (100), *Physical Review B* 47(16) (1993) 10832.
- [11] Z. Cai, M. Kubicek, J.r. Fleig, B. Yildiz, Chemical Heterogeneities on La_{0.6}Sr_{0.4}CoO_{3-δ} Thin Films Correlations to Cathode Surface Activity and Stability, *Chemistry of materials* 24(6) (2012) 1116-1127.